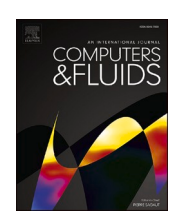
ELSEVIER

Contents lists available at ScienceDirect

Computers and Fluids

journal homepage: www.elsevier.com/locate/compfluid





Enhanced wickability in single- and three-columnar bi-particle size wicks using multiphase lattice Boltzmann method

Mohammad Borumand a, Taehun Lee b, Gisuk Hwang a, *

- ^a Department of Mechanical Engineering, Wichita State University, Wichita, KS 67260, USA
- ^b Department of Mechanical Engineering, The City College of New York, New York City, NY 10031, USA

ARTICLE INFO

Keywords:
Rate-of-rise
Permeability
Capillary flow
Effective capillary meniscus radius
Capillary performance

ABSTRACT

An enhanced wickability, i.e., permeability and capillary pumping capability, is crucial to two-phase thermal management and bio-medical systems, however, it is challenging to enhance them simultaneously. In this study, the enhanced wickability is examined using single-/three-columnar Bi-Particle-Size Wicks (BPSW). The enhanced pore-scale capillary flow with various particle/pore distributions is simulated using a two-phase single component free-energy-based Lattice Boltzmann Method (LBM). The results show that the cumulative liquid saturation of the single- and three-columnar BPSWs (measure of permeability) increases up to 53 and 18%, respectively, while their capillary pressure increases by 76 and 39%, respectively, compared to the Uniform-Particle-Size Wicks (UPSW). The enhancement is related to the fact that the localized larger pores allow for the primary liquid pathways, while the smaller pores increases the capillary pressure simultaneously. The increased pore size ratio leads to 13 and 26% improvement in the cumulative liquid saturation, while it shows the additional 38 and 30% increase in the capillary pressures in the single- and multi-columnar BPSWs. The simulation results provide insights into the optimal thin wick structures for high heat flux two-phase thermal management system by enhancing the wickability through the non-uniform pore sizes.

1. Introduction

Fundamental understandings of transport phenomena in porous media, such as capillary pressure, permeability, diffusivity, are crucial to design and operate various applications including two-phase thermal management [1-4] and renewable power generation systems [5,6], to name a few. For the two-phase thermal management system, the growing trends of integration and miniaturization of the high-power electronic devices and energy conversion systems require innovative thermal management solutions to dissipate the high heat flux for safe and reliable operations. Two-phase cooling systems such as heat pipes and vapor chambers offer high heat flux cooling by using a latent heat compared to conventional single-phase cooling systems. However, their maximum heat dissipation capability is limited by the premature surface dryout of the heated surface from the poor coolant supply through wicks, i.e., viscous-capillary limit [7,8]. The viscous-capillary limit occurs when the viscous pressure drop of the working fluid reaches the maximum capillary pumping capability of the wick structure. To improve the viscous-capillary limit, the permeability and capillary

pumping capability should be enhanced simultaneously, i.e., enhanced wickability.

The wickability has been predominantly studied in uniform pore-size wicks based on the key characteristic geometrical parameters such as porosity, tortuosity, pore sizes, etc. in various wick structures including screen meshes [9,10], grooves [11,12], and sintered particles [13–15]. However, it is difficult to enhance wickability using uniform pore-size wicks due to the pore-size dependent trade-off characteristics between the capillary pressure (inversely proportional to the pore size) and the permeability (proportional to the pore size squared). To address this challenge, various non-uniform pore-size wicks have been explored including bi-porous, bi-disperse, and bi-particle-size wicks, i.e., bi-modal wicks. Byon and Kim [16] have studied the capillary performance (K/r_{eff}) of bi-porous wicks experimentally and analytically by considering the effects of particle and cluster size ratio. The developed semi-analytical model indicated that the optimal capillary performance is obtained when the cluster size is 4-6 times larger than the particle size. Cao et al. [17] have manufactured bi-porous wicks using reaction sintering and pore former dissolution, and found that the capillary performance enhances with the increased pore formers content and cold

Abbreviations: BPSW, Bi-Particle-Size Wicks; LBM, Lattice Boltzmann Method; UPSW, Uni-Particle-Size Wicks.

* Corresponding author.

E-mail address: Gisuk.Hwang@wichita.edu (G. Hwang).

Nomer	nclature	w_1	liquid reservoir width
c _s D g h	speed of sound particle size gravitational acceleration liquid height	Greek sy $ ho$ σ δ_x	density surface tension lattice spacing
h ₀ h ₁ h* K l LP LP*	liquid submerged depth liquid depth dimensionless liquid height permeability pore size large pore larger pore (horizontal direction)	λ κ θ ε ξ ω γ	relaxation time gradient parameter contact angle porosity maximum instantaneous enhancement of BPSW cumulative enhancement of BPSW capillary pressure enhancement of BPSW
LP** L _x L _y r _c r _p s SP SP* SP** t t* UP	larger pore (vertical direction) simulation domain size in x-direction simulation domain size in y-direction capillary meniscus radius particle radius liquid saturation small pore smaller pore (horizontal direction) smaller pore (vertical direction) time dimensionless time uniform pore plate spacing	subscript BPSW c eq max min UPSW p sat u	bi-particle-size wick capillary, contact angle equilibrium maximum minimum uniform-particle-size wick particle or pore saturation uniform vapor

pressure. Egbo et al. [18] have demonstrated the enhanced wickability of bi-particle-size, sintered-particle wicks experimentally by measuring the increased rate of rise due to the increased capillary pressure from the smaller pores and increased permeability from the larger pores. These experimental studies, however, are challenging to examine the pore-scale wickability enhancement mechanism mainly due to limited pore-scale flow visualization methods and manufacturing difficulties for desired pore geometries.

To overcome this challenge, the Lattice Boltzmann Method (LBM) is an ideal study tool for multi-phase, pore-scale flow in complex geometries such as the wick structures [19]. LBM has multiple advantages over conventional interface-tracking methods for two-phase flow in porous media including the Volume of Fluid (VOF) [20,21] and Level Set Method (LSM) [22] such as flexible boundary condition implementation, and low computational cost. However, the previous LBM studies in porous media have focused on two-phase flow characteristics in uniform pore-size porous media, which have no or very limited understandings of the wickability enhancement from non-uniform pore size wicks. Huang et al. [23] simulated immiscible two-phase displacement in complex heterogeneous porous media over a wide range of capillary numbers and viscosity ratios by extending the single-phase LBM boundary conditions and obtained the three typical flow patterns, namely stable displacement, viscous fingering, and capillary fingering. Huang et al. [24] also studied two-phase immiscible displacements driven by constant pressure differentials in randomly-packed spheres and characterized the effects of wettability, viscosity ratio, and capillary number on the relative permeability and the dynamics of displacement. Liu et al. [25,26] employed two-phase LBM with high density ratio to compare immiscible two-phase flow in homogeneous and heterogeneous pore networks by studying the effects of porous media heterogeneity, viscosity ratio, capillary number, and surface wettability on the three main fluid displacement patterns. Recently, Li et al. [27] examined the capillary pumping processes of the reconstructed heterogeneous random wicks at pore scale by employing a 3D two-phase LBM. They investigated the evolutions of two-phase interface and the variations of the transient imbibed liquid volume fraction for the different porosity,

pore structure, and surface wettability to compare with the macroscopic scale homogenous model. However, they only considered uniform pore-size distribution and did not examine the roles of the non-uniform pore size arrangement and characteristic pore-network on the enhanced wickability. More recently, Borumand et al. [28] studied the enhanced wickability in non-uniform pore-size wicks using two-phase LBM, however, they focused on Uni-Particle-Size Wicks (UPSW). In this paper, the enhanced wicking mechanisms are examined using the single- and multi-columnar Bi-Particle Size Wick (BPSW) structure, emphasizing the roles of the particle distribution, pore size ratio, local pore-size distribution, and pore network. The two-phase free-energy-based LBM is employed to predict the enhanced wickability including the rate of rise and capillary liquid front dynamics. This LBM is capable of imposing consistent wetting boundary condition with easy implementation of wetting condition on complex geometry. This paper is organized as follows. In Section 2, the working principle of enhanced wickability in non-uniform pore-size wicks is discussed. In Section 3, the principle of the two-phase LBM including the simulation setup for the UPSW and BPSW and measure of enhanced wickability of the BPSW are presented. In Section 4, the predicted rate-of-rise in the single- and three-columnar UPSW and BPSW are shown including discussions, followed by conclusion.

2. Working principle

The detailed working principle of the enhanced wickability of BPSWs is found in the previous work [28] and only the key description is given below. The enhanced wickability requires the simultaneous improvements of permeability and capillary pumping capability, which are very challenging using the uniform particle size wicks. This technical challenge lies in the nature of the permeability and capillary pumping capability. For example, the permeability of the sintered particle wick is proportional to the particle size squared and the capillary pumping capability is inversely proportional to the capillary meniscus radius (or particle size) [29], as given as

$$K = a \frac{\varepsilon^3 r_p^2}{(1 - \varepsilon)^2} \tag{1}$$

$$p_c = \frac{2\sigma\cos(\theta)}{r_c} \tag{2}$$

where ε is the porosity, a is the constant, and r_D is the particle radius, σ is the surface tension, θ is the contact angle, and r_C is the capillary meniscus radius. To overcome this challenge, the BPSW is employed to develop the non-uniform pore network using the different-size particles for enhanced wickability. To the best of author's knowledge, this is the first study to understand the role of bi-particle size distribution on enhanced wickability using pore-scale capillary flow LBM simulation.

To efficiently study the effects of the BPSW on the enhanced wick-ability, four research hypotheses are identified as follows:

- A The non-uniform pore-size network in both single- and three-columnar BPSWs enhance wickability compared to the uniform pore size wick, while the small pores improve the capillary pressure and large pores enhance the permeability.
- B The wickability further increases as the pore size ratio in the horizontal direction (zig-zag arrangement) increases by additionally opening the flow path through the larger pores and increasing the capillary pressure via smaller pores.
- C The local permeability further improves through even larger pores of the clustered-pores created by both horizontal and vertical pore rearrangement at the expense of the moderate decreased capillary pressure.
- D The wickability enhancement of the clustered-pore BPSW is more pronounced for the three-columnar BPSW compared to the single-columnar BPSW due to the increased locality of the smaller and larger clustered-pores, i.e., improved cluster-pore segregation.

The above hypotheses are examined using the pore-scale two-phase LBM as detailed in Section 3.

3. Methodology

3.1. Lattice Boltzmann method (LBM)

The single-component, two-phase free-energy-based LBM is used in this study, as it is successfully demonstrated to understand the pore-scale capillary flow in the non-uniform pore-size wicks and the important details including the simulation validations are found in the previous work [28,30]. The details of the multi-phase LBM is found in previous works including the stable discretization of the lattice Boltzmann equation [31], elimination of the parasitic currents [32], wall boundary conditions [33], and special boundary treatment at the sharp corners of solid particles [34]. Only the brief key approach is found here.

Fig. 1 shows a schematic of the uniform-particle wick structure for pore-scale LBM simulation including the key parameters, and Table 1 summarizes the values of the LBM parameters used in the present study. Note that the relaxation time in this study is defined such that it does not include the additional correction factor 0.5. The kinematic viscosity, ν , is then calculated by $\lambda = 3/\nu$. We are aware that it is a common practice to report the relaxation time as $\lambda = 3/\nu + 0.5$. Thus, the relaxation time, λ , in the present work is equivalent to 1 in some literature. The boundary conditions of the simulation domain are gradient-free except the bottom boundary where a wall boundary is used. Due to the nature of the symmetric flow along the central vertical line of the simulation domain, only the left half of the simulation domain is solved, i.e., symmetric boundary condition in the center. Liquid depth, h_1 , is large enough to avoid possible liquid supply chocking to the wick, and the liquid reservoir width, w_1 , is large enough to maintain the maximum liquid reservoir level drop below 6%, which is the negligibly small.

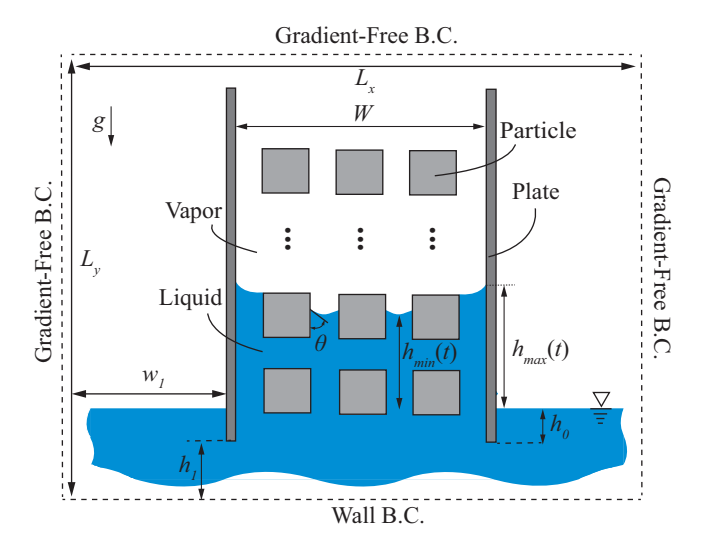


Fig. 1. Schematic of capillary rise in the particle-filled parallel plates, i.e., three-columnar, Uni-Particle-Size Wick (UPSW). The boundary conditions, liquid, vapor, particles, plates, space between the plates, W, maximum liquid height, h_{\max} , minimum liquid height, h_{\min} , liquid-submerged depth, h_0 , liquid depth, h_1 , liquid reservoir width, w_1 , contact angle, θ , gravitational acceleration, g, and domain size, L_x and L_y are also shown.

Table 1
LBM simulation parameters.

LBM Parameter	Magnitude in Lattice Unit			
δ_{x}	1			
δ_t	1			
$ ho_l^{sat}$	1			
$ ho_{v}^{sat}$	0.2			
$ heta_{eq}$	20°			
c_s	$1/\sqrt{3}$			
λ	0.5			
σ	1.365×10^{-3}			
κ	0.0128			
h_O	75			
h_1	200			

3.2. Uni- and bi-particle-size wicks (UPSW and BPSW)

To investigate the aforementioned hypotheses (see Section 2), the rate-of-rise in the single- and multi-columnar particle wicks with Uniand Bi-Particle-Size Wick (UPSW and BPSW) are calculated using LBM, as shown in Fig. 2 and 4, respectively. Fig. 2(a) and Fig. 3(a) show the parallel plates with the spacing of W filled with uni-size square particles, where the pore sizes are uniform near the particles, namely, Uniform Pore (UP), and designated as Cases A0 and B0 for single- and threecolumnar, UPSWs, respectively. Note that these serve as reference cases to measure the enhanced wickability of the BPSWs for three particle arrangement variations (Cases A1-A3 and B1-B3 for single- and three-columnar BPSW, respectively). To study the hypothesis A (see Section 2), the vertically-alternating large and small particle arrangements are designed to have the non-uniform pore network between the particles and the plates, i.e., Large Pores (LP) and Small Pores (SP), as shown in Fig. 2(b) and Fig. 3(b) (Cases A1 and B1 for single- and multicolumnar BPSW, respectively). To study the hypothesis B, the small particles are horizontally re-arranged (zig-zag pore network) aiming at increasing the pore-size ratio, LP*/SP* (or l_4/l_3) = 2.4 compared to LP/ SP (or l_2/l_3) = 1.4 for single-columnar BPSW shown in Fig. 2(c) and (b), and LP*/SP* (or l_6/l_7) = 3.6 compared to LP/SP (or l_3/l_4) = 1.3 for threecolumnar BPSW shown in Fig. 3(c) and (b). Note that for Cases A1-A2 and B1-B2, the pores between the particles in the vertical direction is uniform (UP). To study the hypothesis C, i.e., examining the effects of

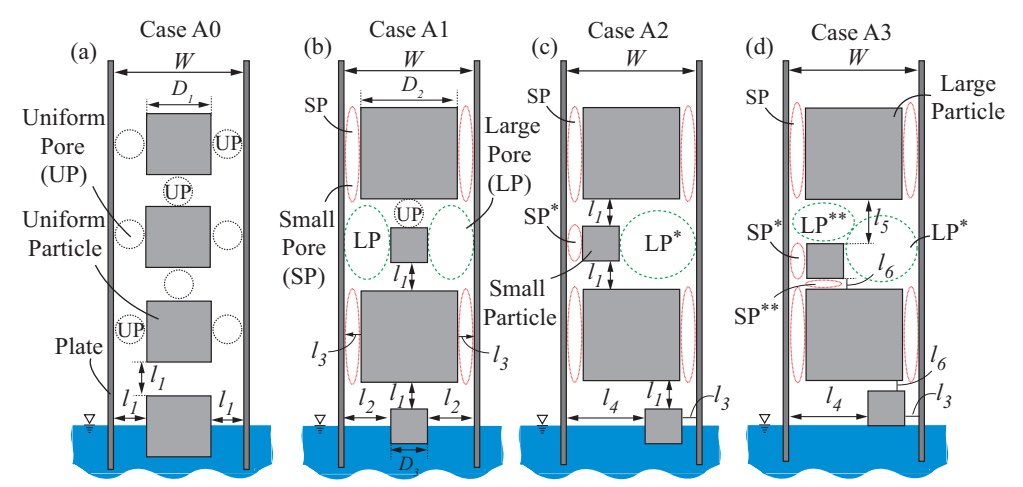


Fig. 2. Single-columnar-particle wick between two parallel plates with the spacing of W and porosity of ε for (a) UPSW (Case AO), BPSWs with (b) small pore-size ratio, (c) increased pore-size ratio (horizontal zig-zag only), and (d) clustered pores (horizontal/vertical zig-zag). The plate spacing, W, particles sizes including the uniform particle, D_1 , large particle, D_2 , and small particle, D_3 , and pore sizes (l_1 to l_7) including the Uniform Pores (UP), Small Pores (SP, SP*, and SP**), and Large Pores (LP, LP*, and LP**) are also shown. The associated geometrical parameters are shown in Table 2.

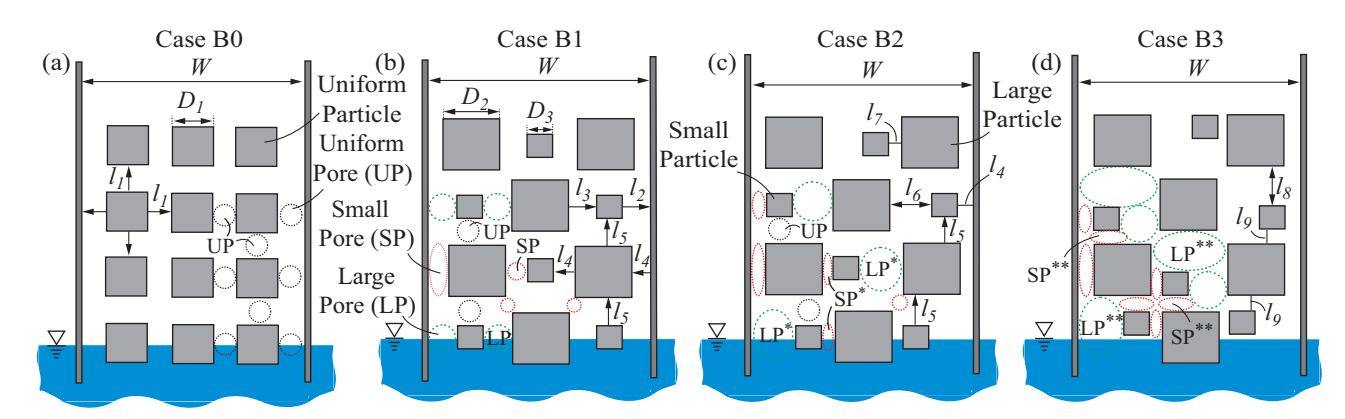


Fig. 3. Three-column-particle wick between the parallel plates with the spacing of W and porosity of ε for (a) UPSW (Case B0), BPSWs with (b) small pore-size ratio, (c) increased pore-size ratio (horizontal zig-zag only), and (d) clustered pores (horizontal/vertical zig-zag). The plate spacing, W, particles sizes including the uniform particle, D_1 , large particle, D_2 , and small particle, D_3 , and pore sizes (l_1 to l_9) including the Uniform Pores (UP), Small Pores (SP, SP*, and SP**), and Large Pores (LP, LP*, and LP**) are also shown. The associated geometrical parameters are shown in Table 3.

non-uniform pore size distribution in both horizontal and vertical directions, the small particles of Cases A2 and B2 are re-arranged accordingly as shown in Fig. 2(d) and Fig. 3(d), i.e., Cases A3 and B3 for single- and three-columnar BPSW, respectively. The resultant pore-size ratio in the vertical direction for the single-columnar BPSW (Case A3) is LP**/SP**(or l_5 / l_6) = 4.4 compared to UP/UP (or l_1 / l_1) = 1 for Cases A2 and A1, and for the three-columnar BPSW (Case B3) LP**/SP** (or l_8/l_9) = 3 compared to UP/UP (or l_5 / l_5) = 1 for Cases B2 and B1. Cases A1/B1, A2/B2, and A3/B3 are herein referred to as the BPSWs with small pore-size ratio, increased pore-size ratio, and clustered-pores, respectively.

Note that we employ 2D wicks with the square particles with two particle sizes between the two parallel plates to understand the porescale enhanced wickability. This may not reflect the complex porenetwork in 3D particle arrangements in practical wick structures, such as sintered particles, 3D mesh, etc. However, the 2D wicks still offers a simple simulation setup to understand the effects of the non-uniform particle size wicks without losing generality, while substantially reducing the computational cost. Table 2 and 3 summarize the LBM simulation parameters for the single- and multi-columnar wicks, respectively, including the parallel plate spacing, W, the porosity, ε , the gravitational acceleration, g, the particle sizes, D_1 - D_3 , the pore sizes, I_1 - I_9 , the liquid reservoir width, W_1 , and the overall domain sizes in both directions, L_X and L_Y .

Similarly, Table 3 also summarizes the simulation parameters of the multi-columnar particle wick.

3.3. Measure of the enhanced wickability of BPSW

The wickability is examined by predicting maximum and minimum dimensionless heights of the capillary meniscus front, $h_{max}^* = h_{max}/W$ and $h_{min}^* = h_{min}/W$, respectively, and liquid saturation, s, i.e., rate-of-rise. To evaluate the wickability enhancement of the BPSW compared to the UPSW, three parameters are introduced, i.e., a maximum instantaneous rate-of-rise enhancement, a cumulative (time integration) rate-of-rise enhancement, and a capillary pressure (equilibrium height) enhancement. The maximum instantaneous rate-of-rise enhancement, ξ is calculated as

$$\xi = \max\left(\frac{\varphi(t^*)_{BPSW} - \varphi(t^*)_{UPSW}}{\varphi(t^*)_{UPSW}}\right) \times 100\%$$
(3)

where φ is either the maximum dimensionless liquid height, h_{max}^* , minimum dimensionless liquid height, h_{min}^* , or liquid saturation, s, respectively. In other words, Eq. (3) finds the normalized difference between h_{max}^* , h_{min}^* , and s of the BPSW and UPSW for the entire capillary rise and reports the maximum value for each of these three parameters as the maximum achieved enhancement. The cumulative (time integrated) rate-of-rise enhancement, ω is given as

$$\omega = \frac{\int_0^{t_{eq}^*} \varphi(t^*)_{BPSW} dt^* - \int_0^{t_{eq}^*} \varphi(t^*)_{UPSW} dt^*}{\int_0^{t_{eq}^*} \varphi(t^*)_{UPSW} dt^*} \times 100\%$$
 (4)

where t^*_{eq} is the dimensionless time for the equilibrium height. The

Table 2

Summary of the LBM simulation parameters for single-columnar UPSW and BPSW shown in Fig. 2(a)-(d) including the parallel plate spacing, W, porosity, ε , gravitational acceleration, g, square particle sizes, D_1 - D_3 , particle size ratio, D_r , pore sizes, l_1 - l_7 , the small pore-size ratio, i.e., LP/SP, the increased pore size ratio, i.e., LP*/SP*, the pore size ratio (in the flow direction) for the clustered-pore wick, i.e., LP**/SP**, the domain size from the side boundaries to the external surface of the plates, W_1 , and the overall domain sizes in both directions, L_x and L_y .

Simulation parameters	Magnitude, Lattice Unit				
	Case A0	Cases A1, A2 and A3			
W	156	156			
ε	0.65	0.65			
$g \times 10^7$	1	1			
D_1	80	-			
D_2	_	98			
D_3	-	58			
$D_{\rm r} = D_1/D_1 \text{ or } D_2/D_3$	1	1.7			
l ₁ (UP)	38	-			
l_2 (LP)	_	49			
l ₃ (SP, SP*)	_	29			
LP/SP	_	1.4			
l ₄ (LP*)	_	69			
LP*/SP*	-	2.4			
l ₅ (LP**)	-	62			
l ₆ (SP**)	_	14			
LP**/SP**	_	4.4			
w_1	1,000	1,000			
Lx	2,180	2,180			
Ly	609	609			

Table 3

Summary of the LBM simulation parameters for multi-columnar, UPSW and BPSW shown in Fig. 3(a)-(d) including the parallel plate spacing, W, porosity, ε , gravitational acceleration, g, square particle sizes, D_1 - D_3 , particle size ratio, D_r , pore sizes, l_1 - l_9 , the small pore-size ratio, i.e., LP/SP, the increased pore size ratio, i.e., LP*/SP*, the pore size ratio in the flow direction for the clustered-pore wick, i.e., LP*/SP**, the domain size from the side boundaries to the external surface of the plates, W_1 , and the overall domain sizes in both directions, L_x and L_y .

Simulation parameters	Magnitude, Lat Case B0	tice Unit Case B1, B2, and B3
W	314	314
ε	0.65	0.65
$g \times 10^7$	1.35	1.35
D_1	58	_
D_2	_	76
D_3	_	38
$D_{\rm r} = D_1/D_1 \text{ or } D_2/D_3$	1	2
l ₁ (UP)	35	_
l ₂ (LP)	-	41
l ₃ (LP)	-	40
l ₄ (SP)	-	31
LP/SP	-	1.3
l ₅ (UP)	-	38
l ₆ (LP*)	-	50
l ₇ (SP*)	-	14
LP*/SP*	-	3.6
l ₈ (LP)	-	57
l ₉ (SP)	-	19
LP**/SP**	-	3.0
w_1	1,500	1,500
L_x	3,314	3,314
L_{γ}	609	609

equilibrium dimensionless time is determined at the time when both maximum and minimum heights become constant over at least 100 dimensionless time periods, i.e., $\Delta t^* > 100$.

The maximum capillary pressure enhancement, γ is predicted as

$$\gamma = \frac{\varphi(t^*)_{BPSW,eq} - \varphi(t^*)_{UPSW,eq}}{\varphi(t^*)_{UPSW,eq}} \times 100\%$$
 (5)

where φ is either the maximum dimensionless liquid height, h^*_{max} , minimum dimensionless liquid height, h^*_{min} , or liquid saturation, s at equilibrium state, respectively. The summary of the predicted wickability enhancements of BPSWs is found in Section 4.3.

4. Results and discussion

4.1. Single-columnar, uni- and bi-particle-size wicks (UPSW and BPSWs)

4.1.1. BPSW with small pore size ratio (Case A1) vs UPSW (Case A0)

To understand the effects of the non-uniform pore network in the single-columnar BPSW (Case A1) on enhanced wickability, the LBM predicted rate-of-rise is compared with that of the single-columnar UPSW (Case A0, reference case). Fig. 4 shows the LBM simulation snapshots of the rate-of-rise from the initial time to equilibrium state for Case A0 [see Fig. 2(a)]. Note that the predicted rate-of-rise in the UPSW (Fig. 4) is similar to the previous work [28], however, here a different gravitational acceleration value, g, is used due to the different particle/pore sizes for desired equilibrium height. Fig. 4(a) illustrates the liquid height within the two plates at $t^* = 0$ which stays in the same level as the liquid pool. At $t^* = 0.5$, Fig. 4(b) shows that the capillary meniscus forms where the liquid equally fills the pore space between the particle and plates which in turn results in a sharp rate-of-rise. At $t^* = 12$, Fig. 4 (c) illustrates that one side of the two capillary menisci are pinned to the sharp particle upper corners, i.e., the minimum liquid height, while the maximum liquid height continues to rise along the inner plate surfaces. Note that the capillary meniscus radius gradually increases between t^* = 0.5 and 12, i.e., the capillary pressure decreases during the pinning process due to the increasing capillary meniscus radius, which in turn delays the rate-of-rise [35]. At $t^* = 45$, Fig. 4(d) shows that the minimum liquid height has detached from the upper particle corner, i.e., meniscus depinning, followed by slow lateral liquid spread over the top surface of the particle, i.e., stick-slip flow. Meanwhile, the maximum liquid height continues to rise along the inner plate surface increases. At $t^* = 92$, Fig. 4(e) shows that the left and right menisci have bridged to form a new capillary meniscus across the two plates. At $t^* = 110$, Fig. 4 (f) illustrates that the capillary menisci interact with the bottom side of the second particle to form the new small capillary menisci, which results in the second sharp rate-of-rise between the particle and the plate at $t^* = 115$ [Fig. 4(g)]. At $t^* = 110$ [Fig. 4(f)], due to sudden, two additional capillary menisci formation from the strong interaction between the capillary meniscus front and the bottom corners of the third particle, an isolated vapor is formed by being "trapped" between two capillary menisci. The isolated vapor gradually reduces the size by the vapor-liquid phase change, facilitated by the strong surface-capillary meniscus front interaction, until it completely disappears. The liquid continues to rise until it reaches the top surface of the second particle, and then it does not significantly change the height due to the meniscus pinning. At $t^* = 1,350$, Fig. 4(h) shows that the liquid front reaches the equilibrium state. Note that the h^*_{\max} and h^*_{\min} at the equilibrium state is smaller than the expected equilibrium height from the force balance between the capillary pressure and hydrostatic pressure due to the reduced pressure from the pinning effect.

Similarly, Fig. 5 shows the LBM simulation snapshots of the rate-of-rise for Case A1 [see Fig. 2(b)]. Fig. 5(m) shows the formation of the capillary meniscus between the small particle and the plates at $t^*=1$, i. e., first sharp-rate-of-rise. At $t^*=32$, Fig. 5(n) shows that the inner parts of the menisci (minimum height) are pinned to the particle top corners, i.e., pinning, while the maximum height rises along the inner surface of the parallel plates. Fig. 5(o) shows the stick-slip flow over the top surface of the small particle while the maximum liquid height continues to rise along the inner plate surface. At $t^*=44$, Fig. 5(p) shows an early capillary rise compared to Case A0 [Fig. 4(d)-(e)], i.e., enhanced wickability, by stronger interactions between the capillary front and bottom corners of the second layer particle. Next, this leads to the formation of

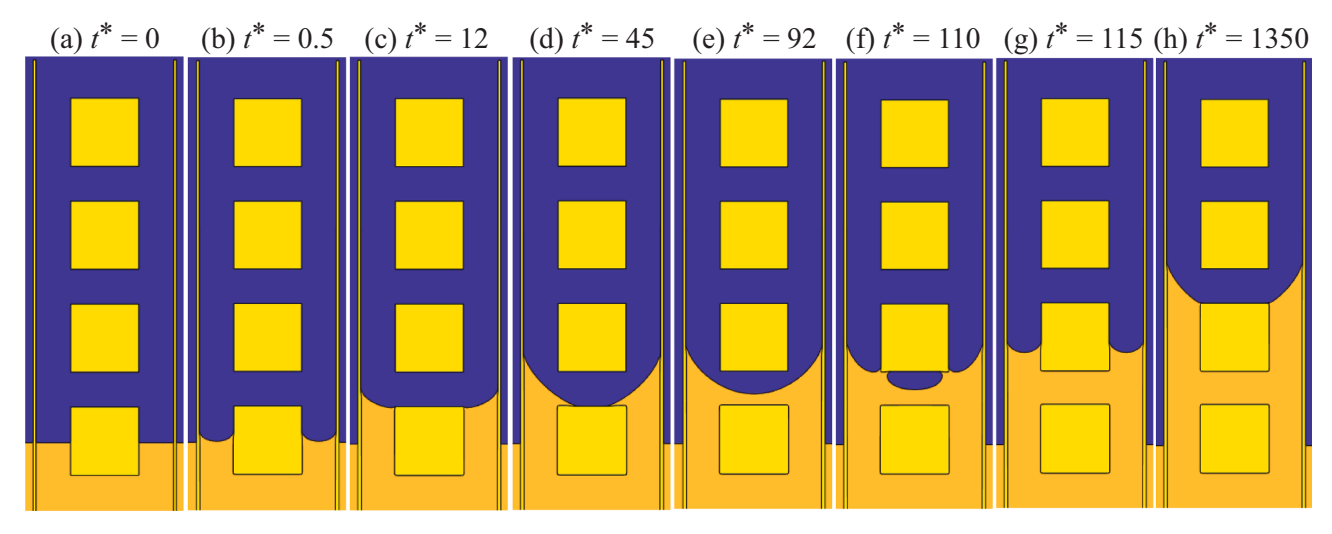


Fig. 4. Snapshots of rate-of-rise in single-columnar, UPSW (Case A0) from (a) the initial time, $t^* = 0$, to (h) the equilibrium state $t^* = 1,350$. The dimensionless time, t^* , corresponding to each snapshot is also shown.

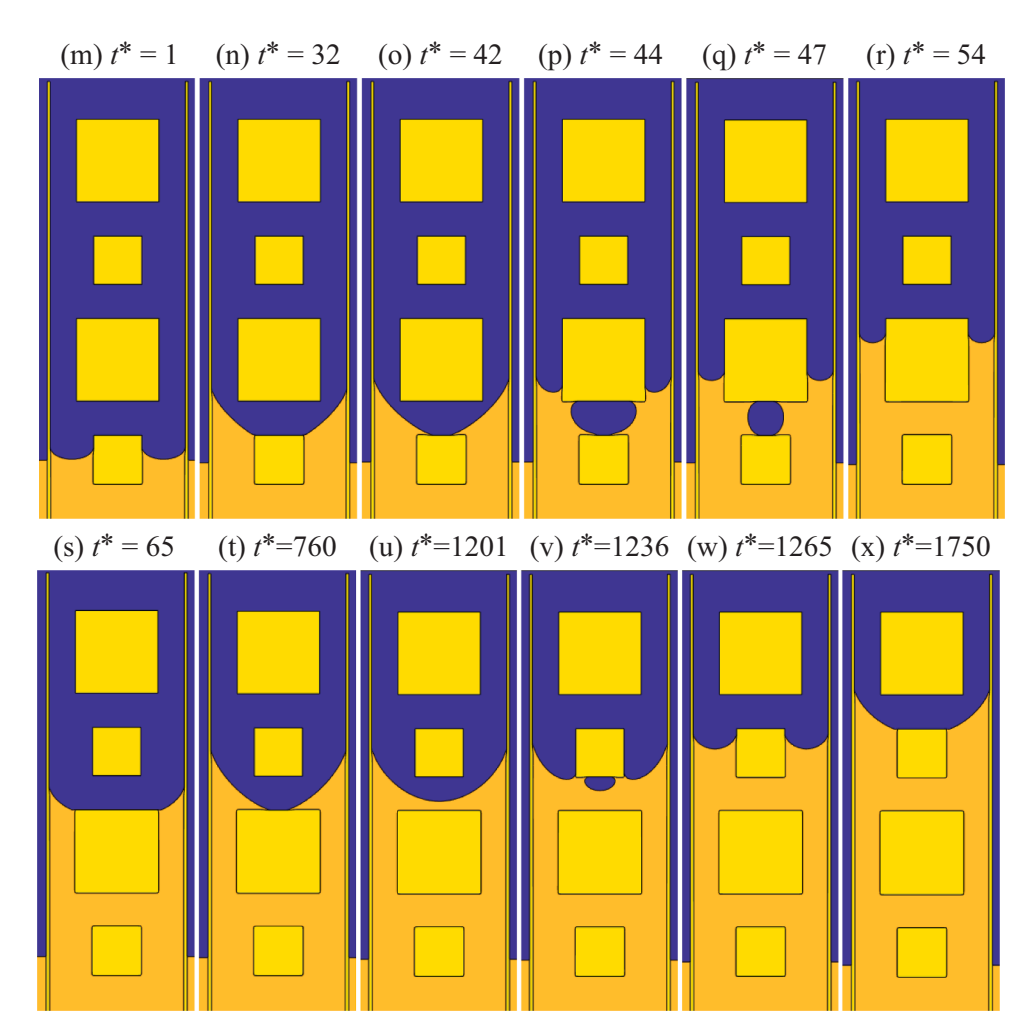


Fig. 5. Snapshots of rate-of-rise in single-columnar, bi-particle-size wick with small pore size ratio (Case A1) from (m) the first sharp rate-of-rise at $t^* = 1$ to (x) the equilibrium state $t^* = 1,750$. The dimensionless time, t^* , corresponding to each snapshot is also shown.

the new menisci with small radii, and the liquid fills the remaining space between the small and large particles, while the maximum liquid height starts the second sharp rate-of-rise between the large particle and plates, i.e., Fig. 5(q) and (r) at $t^* = 47$ and 54, respectively. At $t^* = 65$, Fig. 5(s)

shows that the capillary meniscus front continuously rises and pins at the sharp upper corners of the second particle. Then, it depins to flow over the top surface of the large particle, i.e., stick-slip flow, as shown in Fig. 5(t) at $t^* = 760$, followed by the continuous capillary rise, while

being detached from the top surface of the large particle at $t^*=1201$, as shown in Fig. 5(u). This additional capillary rise momentum is generated by the increased capillary pressure from the smaller pores between the large particle in the second layer and plates in BPSW (Case A1), while the capillary font stops in the top of the second particle at the equilibrium for the UPSW, i.e., Case A0 [see Fig. 4(h)]. The similar capillary rise to Fig. 5(p) to (s) is observed in Fig. 5(v) to (x) until it reaches the equilibrium height at $t^*=1750$, as shown Fig. 5(x). Note that the equilibrium height of Case A1 is larger than that of Case A0 due to the smaller pore size.

Fig. 6(a) and (b) compare the LBM predicted maximum and minimum dimensionless liquid heights, h_{max}^* , and h_{min}^* , respectively, as a function of dimensionless time, t^* , for single-columnar, UPSW (Case A0) and BPSW with small pore size ratio (Case A1) at given porosity $\varepsilon = 0.65$ and parallel plate spacing $W = 156 \delta x$. The time label used in Fig. 4 and Fig. 5, and the locations of the 4 particles for Cases A0 and A1 are also shown, and the insets magnify the early stages of the rate-of-rise for improved readability. Note that some time labels are omitted for improved readability. To explain the mechanism of enhanced wickability, we focus on the sharp capillary rises for two time periods, t^* \land 150 and t^* 1250, while the capillary meniscus rises continuously at 150 $< t^*$ < 1250. The detailed pore-scale descriptions of the rate-of-rise are found above, and here only the main wickability enhancement mechanisms are discussed. At $t^* < 150$, the two step-wise capillary rises, i.e., a sharp capillary rise followed by a plateau and another sharp capillary rise, are observed for both cases, but for Case A1, the early capillary rise is achieved at (p) to (s) for both maximum and minimum liquid heights. This enhanced wickability is related to not only the increased local permeability from the large pores between the first-layer particle of Case A1 and the plates, but also the additional capillary rise momentum from the increased capillary pressure by the smaller pores between the second-layer particle of Case A1 and the plates, i.e., the stronger interaction of the capillary meniscus front with the bottom corners of the particle at Fig. 5(p).

At $150 < t^* < 1,250$, Case A1 continues to rise due to the larger capillary pumping from the small pore between the second-layer particle and the plates, while Case A0 reaches equilibrium height due to smaller capillary pressure. Note that no capillary rise in the minimum height, h_{min}^* , in certain time intervals such as points (n) to (o) or (s) to (t) is related to the pinning, depinning, and stick-slip flow near the sharp corners of the particles, while during the same time interval the maximum height, h_{max}^* , continues to rise slowly along the inner surfaces of the two plates. At $t^* > 1,250$, the Case A1 shows the additional sharp capillary rise, i.e., (u) and (w), due to the larger local permeability from the larger pores between the third-layer smaller particle and two plates, followed by the equilibrium height at the top of the third-layer particle, i.e., point (x). Fig. 6(c) compares the liquid saturation, s, as a function of dimensionless time, t^* , for Cases A0 and A1, to further understand the enhanced wickability via the time-dependent liquid-filled pore volume which contains both the maximum and minimum heights in a single parameter. Two significant liquid saturation increases of Case A1 are observed. One is the point (n) due to the larger local permeability from the large pores in the bottom side of the BPSW followed by the strong capillary rise momentum from the meniscus-particle interaction at point (p). The other is the points (u) and (w) due to the similar reasons.

The predicted maximum instantaneous and cumulative rate-of-rise enhancements and capillary pressure enhancements of Case A1 using Eqs. (3) to (5) are $\xi = 309\%$ (for h^*_{\min} at $t^* = 78$), $\omega = 53\%$ (in s), and $\gamma = 76\%$ (in s), and other detailed enhancement predictions and comparisons are summarized in Section 4.3.

4.1.2. BPSW with increased pore size ratio (Case A2)

This section studies the effects of the increased pore size ratio of the single-columnar BPSW [Case A2, horizontally zig-zag arrangement, Fig. 2(c)] on enhanced wickability by comparing the rate-of-rise with the single-columnar BPSW with small pore-size ratio [Case A1, Fig. 2

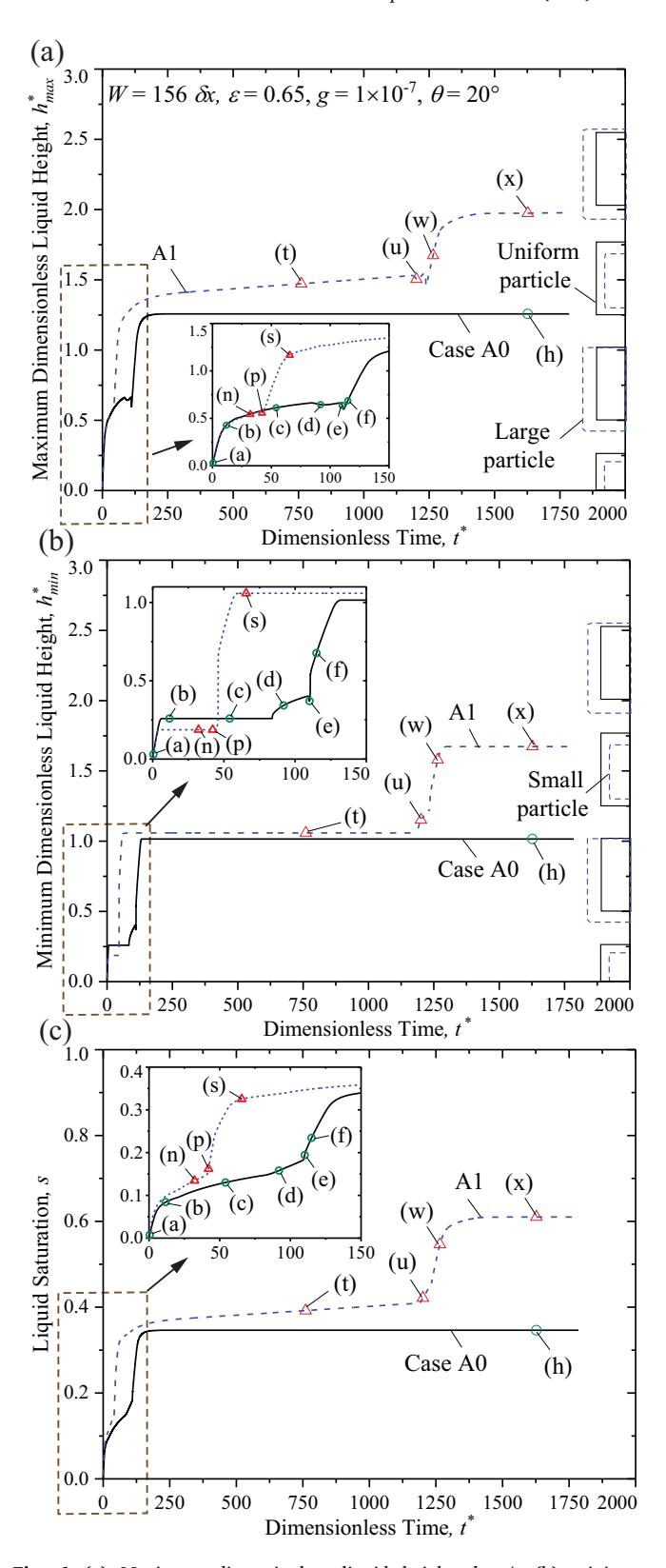


Fig. 6. (a) Maximum dimensionless liquid height, h_{max}^* , (b) minimum dimensionless liquid height, h_{min}^* , and (c) liquid saturation, s, as a function of dimensionless time, t^* , for single-columnar, UPSW (Case A0) and BPSW with small pore size ratio (Case A1) at given porosity $\varepsilon=0.65$ and parallel plate spacing $W=156~\delta x$.

(b)]. Fig. 7(a) shows the initial liquid height, followed by the first sharp capillary rise at $t^*=2$, i.e., Fig. 7(b). Note that the maximum height in the large pore is slightly higher than that of the small pore, because the increased local permeability with the reduced capillary pressure from the larger pore allows for the improved liquid rise momentum compared to the reduced local permeability with the improved capillary pressure from the small pore. At $t^*=8.5$, Fig. 7(c) shows that the maximum liquid height in the left pore is higher than of the right pore due to the larger local permeability from the large pore, while maintaining the same minimum liquid height at the top corner of the first-layer particle, i.e., pinning. At $t^*=16$, Fig. 7(d) shows that the right capillary meniscus depins earlier than the left one due to the high capillary pressure from the small pore, while the left one continues to quickly rise along the inner plate surface, i.e., larger permeability, without depinning.

At $t^*=19.7$, Fig. 7(e) illustrates that the left capillary meniscus interacts with the bottom left corner of the second-layer particle, which in turn forms two smaller menisci for further vertical and horizontal capillary flows. This horizontal zig-zag particle rearrangement allows for the early vertical capillary rise compared to that of Case A1 [see Fig. 5(o)]. At $t^*=24.2$, Fig. 7(f) shows that the left smaller pore allows for the second sharp capillary rise due to the increased capillary pressure, while the pore between the first and second-layer particle provides the horizontal capillary flow resulting in quick detachment of the minimum height from the top surface of the first-layer particle. At $t^*=34$, Fig. 7(g) shows that the liquid in the left pore reaches the top surface of the second-layer particle, and the liquid in the right pore, i.e., the minimum height, quickly rises due to the increased capillary pressure

from the smaller pore. At $t^* = 352$, Fig. 7(h) shows that both the left and right capillary menisci depin and flow over the top surface of the secondlayer particle, i.e., stick-slip flow. At $t^* = 1,001$, Fig. 7(i) shows that the small pore between the third-layer particle and the left plate [SP* in Fig. 2(c)] allows for stronger meniscus-particle interaction, resulting in the, wickability enhancement compared to Case A1 [see Fig. 5(v)]. . At $t^* = 1,041$, Fig. 7(j) shows that the left meniscus quickly rises due to the increased capillary pressure from the smaller pore, while the right meniscus fills the pore between the second- and third-layer particles, leading to minimum height detachment. At $t^* = 1,312$, both the left and right menisci pin at the third-layer particle corners as shown in Fig. 7(k), before the further capillary rise. At $t^* = 1,823$, Fig. 7(1) shows that left meniscus depins due to the large capillary pressure from the small pore to flow over the top surface of the third-layer particle, while the right meniscus continues to pin since the small capillary pressure from the large pore [LP* in Fig. 2(c)] does not overcome the required capillary pressure for further rise. At $t^* = 2,375$, Fig. 7(m) shows that the left smaller pores assists to form two smaller menisci for further capillary rises vertically and horizontally as shown in Fig. 7(n) at $t^* = 2,540$, followed by the additional vertical capillary rise through the small right pore as shown in Fig. 7(o) at $t^* = 2.623$. Finally, it reaches the equilibrium height at $t^* = 3,000$, i.e., Fig. 7(p).

To understand the effects of increased pore size ratio on enhanced wickability of single-columnar BPSW, Fig. 8(a), (b), and (c) compare the LBM predicted maximum and minimum dimensionless liquid heights, h_{max}^* and h_{min}^* , and liquid saturation, s, respectively, as a function of dimensionless time, t^* , for single-columnar BPSW wicks with small

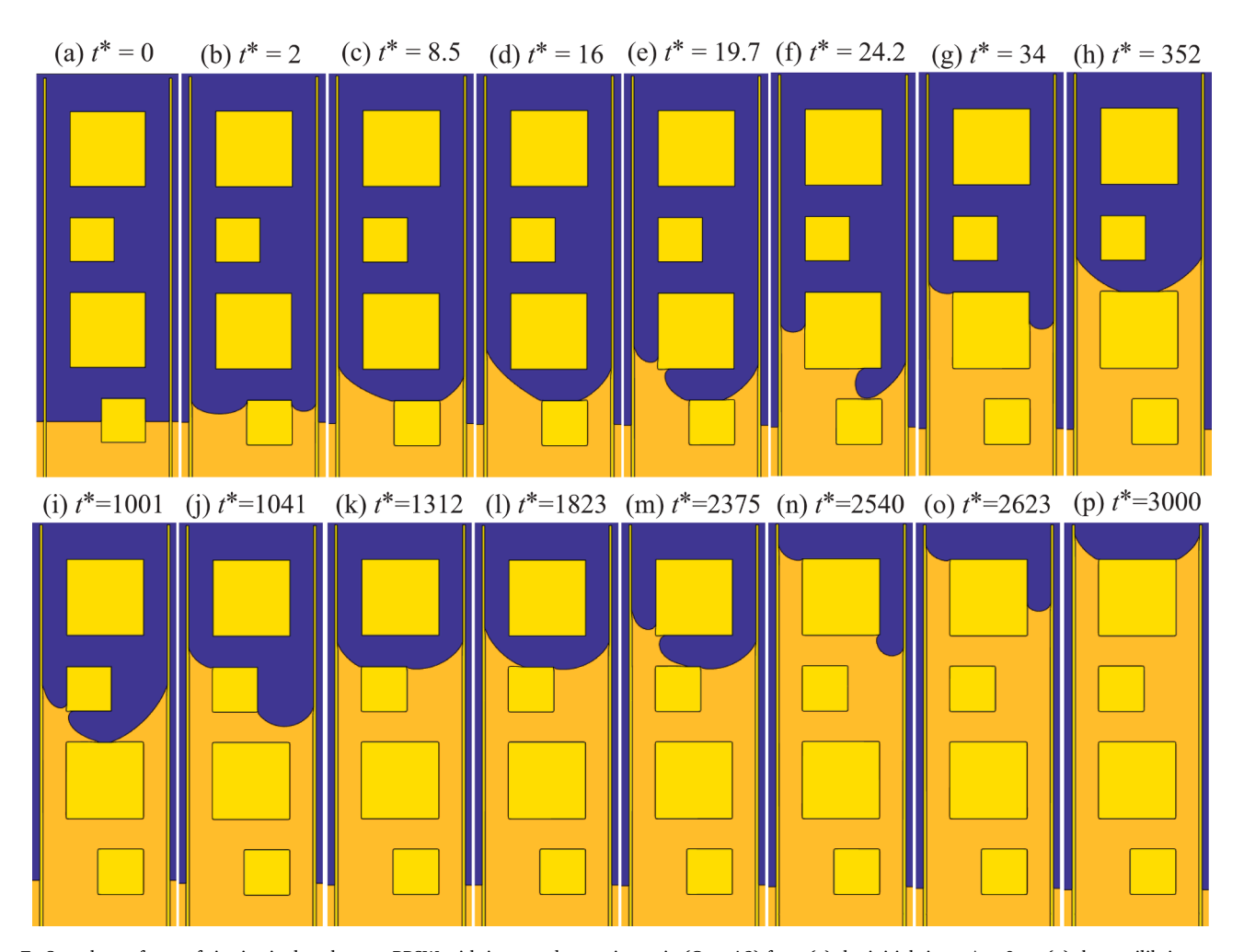


Fig. 7. Snapshots of rate-of-rise in single-columnar BPSW with increased pore size ratio (Case A2) from (a) the initial time, $t^* = 0$, to (p) the equilibrium state $t^* = 3,000$. The dimensionless time, t^* , corresponding to each snapshot is also shown.

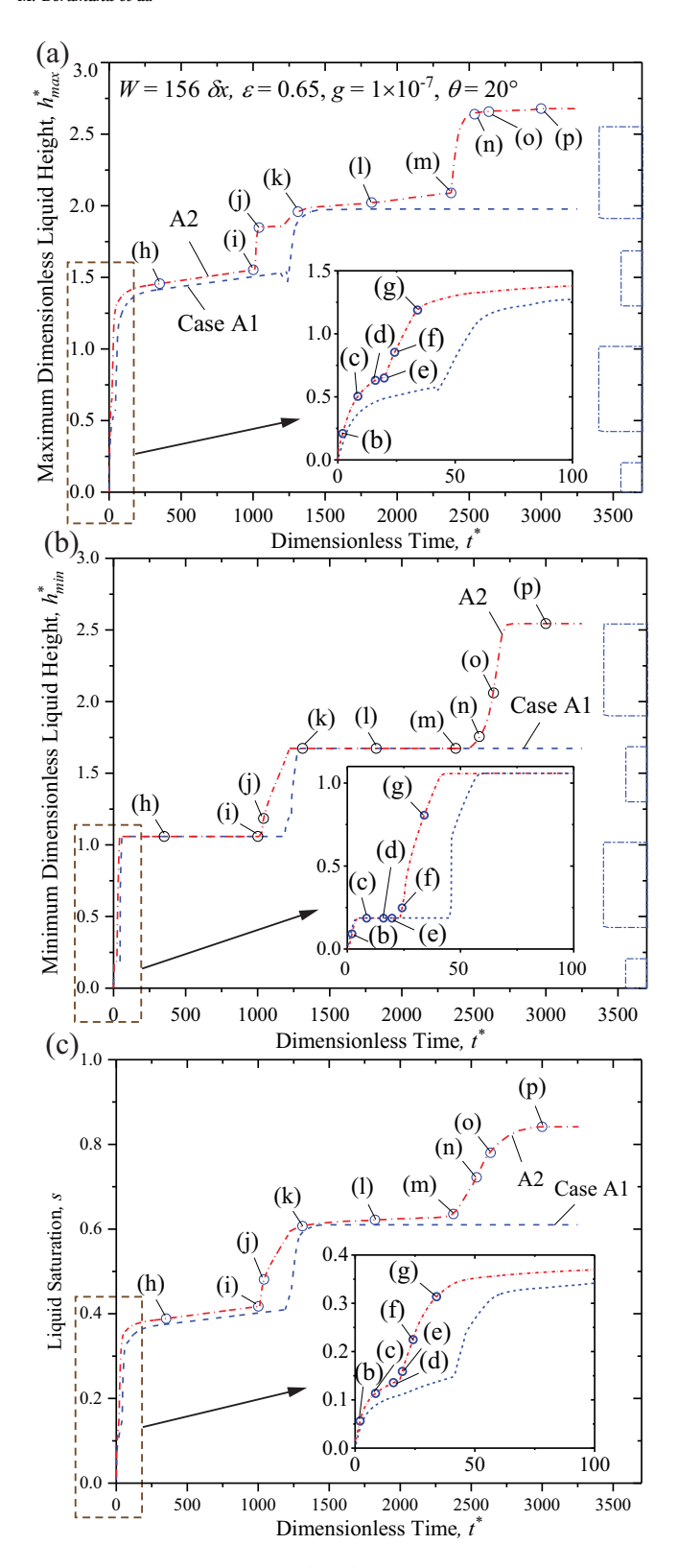


Fig. 8. (a) Maximum dimensionless liquid height, h_{max}^* , (b) minimum dimensionless liquid height, h_{min}^* , and (c) liquid saturation, s, as a function of dimensionless time, t^* , for single-columnar BPSW with small and large pore size ratios, i.e., Case A1 and A2, respectively, at given porosity $\varepsilon=0.65$ and parallel plate spacing W=156 δx .

(Case A1) and increased pore size ratio (Case A2, horizontal zig-zag particle rearrangement), at given porosity $\varepsilon = 0.65$ and parallel plate spacing $W = 156 \delta x$. The time labels used in Fig. 7, the location of the 4 particles for Cases A1 and A2, and the insets are also shown. The enhanced wickability of the increased pore-size ratio BPSW (Case A2) mainly stems from two step-wise early capillary rises at $t^* = 24.2$ [point (f)], and 1,001 [(i)] and additional capillary rise at $t^* = 2,375$ [(m)] from non-uniform pore networks by the horizontal zig-zag particle rearrangement, compared to the Case A1. At $t^* = 24.2$, the first early (sharp) capillary rise is triggered by the stronger interaction between the extended capillary meniscus at large pore of the first layer particle and the bottom left corner of the second layer particle (large permeability from the large pore), followed by the sudden vertical capillary rise through the smaller pore between the left plate and the second-layer particle (large capillary pumping from the small pore). Similarly, at t^* = 1.001 and 2,375, the second and third strong capillary rise is observed primarily due to the horizontal zig-zag particle rearrangement, i.e., enhanced capillary pumping and liquid flow from SP* and LP* in Fig. 2 (c), respectively.

The predicted maximum instantaneous and cumulative rate-of-rise enhancements and capillary pressure enhancement of Case A2 compared to Case A1 using Eqs. (3) to (5) are $\xi=465\%$ (for h^*_{\min} at equilibrium, i.e., $t^*=44$), $\omega=14\%$ (in h^*_{\max}), and $\gamma=52\%$ (in h^*_{\min}), and other detailed enhancement predictions and comparisons are summarized in Section 4.3.

4.1.3. BPSW with clustered-pores (Case A3)

To understand the clustered-pore effects on enhanced wickability of single-columnar BPSW (Case A3, vertical/horizontal zig-zag particle rearrangement), the LBM predicted rate-of-rise is compared with that of Case A2, i.e., BPSW without clustered-pores (horizontal zig-zag particle rearrangement only). Fig. 9 shows the LBM simulation snapshots of the rate-of-rise from the initial time to equilibrium state for Case A3 [see Fig. 2(d)]. While the overall pore-scale capillary flow for Case A3 for 0 < $t^* < 291$, i.e., Fig. 9(a)-(1), is similar to those of Case A2, the clusteredpores in Case A3 not only facilitate the meniscus-particle interaction at $t^* = 9$, i.e., Fig. 9(c), compared with $t^* = 19.7$, Fig. 7(e), but also promote the minimum height detachment at $t^* = 15$, Fig. 9(e), compared with $t^* = 24.2$, Fig. 7(f), due to the enhanced local permeability from the large pore between the first-layer particle and the left plate as well as the improved capillary pumping from the smaller pore between the firstand second-layer particles. The clustered-pores further enhance the rateof-rise due to the stronger meniscus-particle interaction as shown in Fig. 9(h) by providing the capillary pumping capability which results in the sharp capillary rise until the liquid reaches the level of the top surface of the third-layer particle at $t^* = 291$, i.e., point (l) in Fig. 9 compared to $t^* = 1312$ in Fig. 7(k), i.e., enhanced wickability from the clustered-pores. On the other hand, the large clustered-pores between the third- and fourth-layer particles in Case A3 [see LP* and LP** in Fig. 2(d)] reduce the capillary pressure, i.e., the liquid prematurely stops in the large clustered-pores at $t^* = 2,000$, i.e., Fig. 9(p), compared to Fig. 7(p) at $t^* = 3,000$, in which the liquid for Case A2 reaches the top surface of the fourth layer particle due to the large capillary pressure from the small pore between the third- and fourth-layer particles.

To further understand the effects of clustered-pores on enhanced wickability of BPSW, Fig. 10(a), (b), and (c) compare the LBM predicted maximum and minimum dimensionless liquid heights, h_{max} * and h_{min} *, and liquid saturation, s, respectively, as a function of dimensionless time, t*, for single-columnar BPSW with clustered-pores (Case A3, vertical/horizontal zig-zag particle rearrangement) and single-columnar BPSW without clustered-pores (Case A2, horizontal zig-zag particle rearrangement only), at given porosity $\varepsilon = 0.65$ and parallel plate spacing $W = 156 \, \delta x$. The time labels used in Fig. 10, the location of the 4 particles for Cases A3 and A2, and the insets are also shown.

The large pore between the first-layer particle and the plate enhances the local permeability [e.g., see enhanced liquid saturation at point (c)

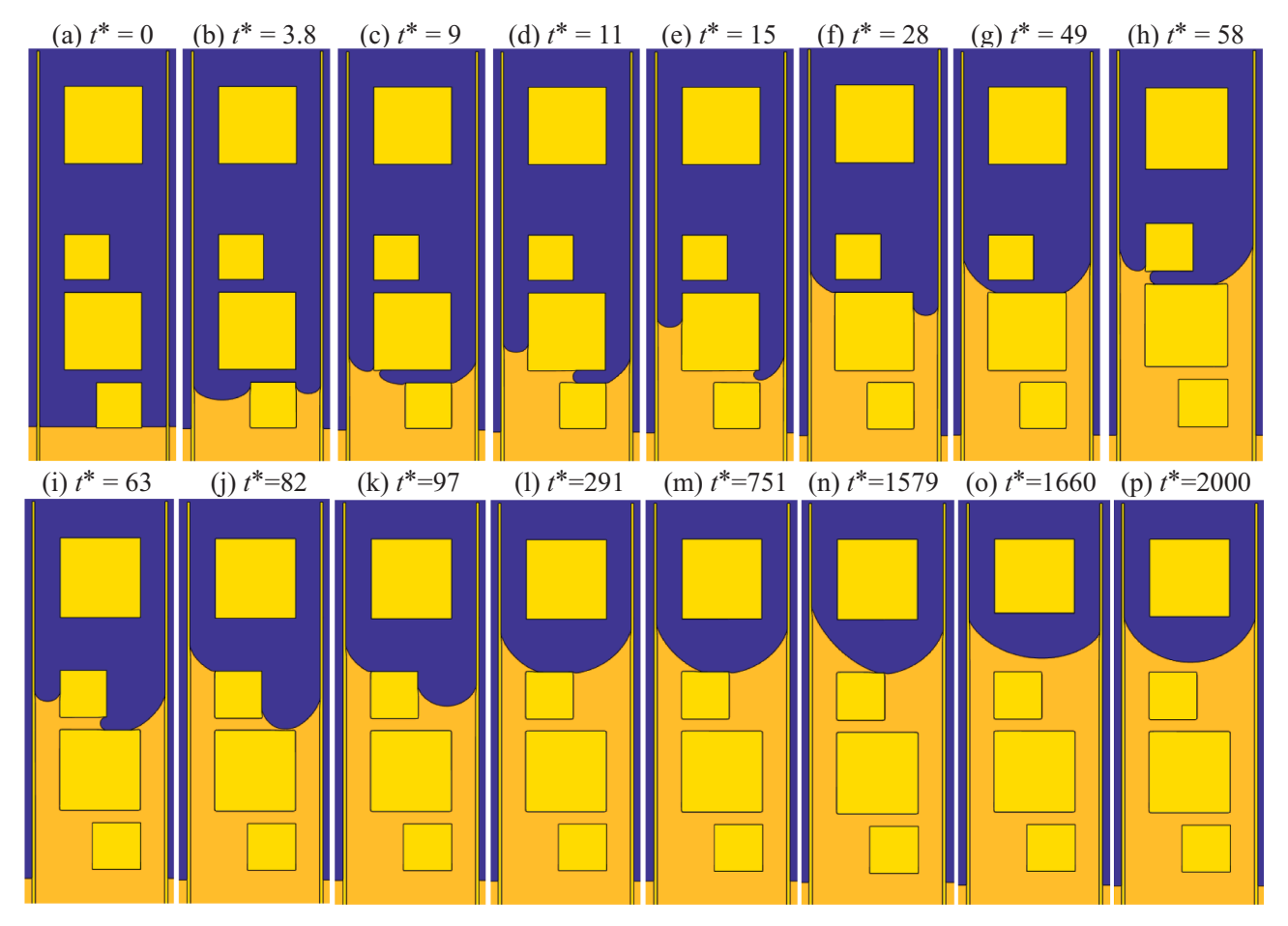


Fig. 9. Snapshots of rate-of-rise in single-columnar BPSW with clustered-pores (Case A3) from (a) the initial time, $t^* = 0$, to (p) the equilibrium state, $t^* = 2000$. The dimensionless time, t^* , corresponding to each of the snapshots are also shown.

in Fig. 10(c)], while the small pore between the first- and second-layer particle provide capillary pumping for sharp capillary rise at $11 < t^* < 28$ [points (d)-(f) in Fig. 10(a)-(c)]. Furthermore, the clusters of small pores between the second- and third-layer particle [see SP* and SP** in Fig. 2(d)] provide the capillary pumping capability for the second sharp capillary rise at $58 < t^* < 63$ [points (h)-(i)], and the large pore between the third-layer particle and the right plate [see LP* in Fig. 2(d)] allows the liquid to rise to the top surface of the third-layer particle, i.e., improved local permeability at $82 < t^* < 291$ [points (j)-(l)]. The clusters of large pores slow down the capillary rise at $t^* > 291$ [point (l) – (p)], since the reduced capillary pressure does not overcome the increased hydrostatic pressure, i.e., equilibrium state is prematurely reached at $t^* = 2,000$ [point (p)].

Compared to Case A2, the clustered-pores in Case A3 results in 60, 293, and 85% instantaneous enhancement for the maximum and minimum height and liquid saturation at $t^*=19$, 23, and 19 respectively. While for the first half of the rate-of-rise, i.e., $t^*<1,000$, the clustered-pores cumulatively enhance the maximum and minimum height and liquid saturation by 23, 41, and 30%, respectively, the cumulative capillary rise is similar to that of Case A2. However, the capillary pressure of Case A3 decreases by $\gamma=29,37$, and 32% for the maximum and minimum height and liquid saturation, respectively, compared to that of Case A2, due to the larger pore clusters in the top part of BPSW. The detailed enhancement predictions and comparisons are summarized in Section 4.3.

4.2. Three-columnar, uni- and bi-particle-size wicks (UPSW and BPSWs)

4.2.1. BPSW with small pore size ratio (Case B1) vs UPSW (Case B0)

To understand the effects of the non-uniform pore network in the three-columnar BPSW (Case B1) on enhanced wickability, the LBM predicted rate-of-rise is compared with that of the three-columnar UPSW (Case A0, reference case).

Fig. 11 shows the LBM simulation snapshots of the rate-of-rise from the initial time to equilibrium state for Case B0 [see Fig. 3(a)]. Fig. 11 (a)-(f) illustrate the initial time at (a), the first sharp capillary rise at (b), end of the first sharp capillary rise and start of the meniscus slow-down process due to the lost curvature at (c), pinned meniscus at (d), depinned meniscus at (e), and stick-slip flow at (f), respectively. At $t^* = 18.5$, Fig. 11(b) shows the meniscus-particle interaction, followed by the second sharp capillary rise both in vertical and horizontal directions at $t^* = 19.2 - 21.5$, i.e., Fig. 11(h)-(j). At $t^* = 28.7$, Fig. 11(k) shows that the maximum height located at the inner plate surface reaches its highest point, while the central capillary meniscus rises slowly due to the stick slip flow. Note that the minimum height, h_{min}^* , remains unchanged at the level of the top surface of the first-layer particles between Fig. 11(c)-(k), i.e., $t^* = 0.3$ - 28.7. At $t^* = 31.4$, Fig. 11(1) shows that the minimum height finally detaches from the first-layer particle surface, followed by the meniscus-particle interaction at points (m)-(n) and the final sharp capillary rise at point (o). At $t^* = 100$, Fig. 11(p) shows that the equilibrium state reaches for both maximum and minimum height, since the pore size between the plates and the adjacent particles, i.e., the left and right particles, is not small enough to provide capillary pumping capability for liquid rise to the third particle layer.

Similarly, Fig. 12 shows the LBM simulation snapshots of the rate-of-

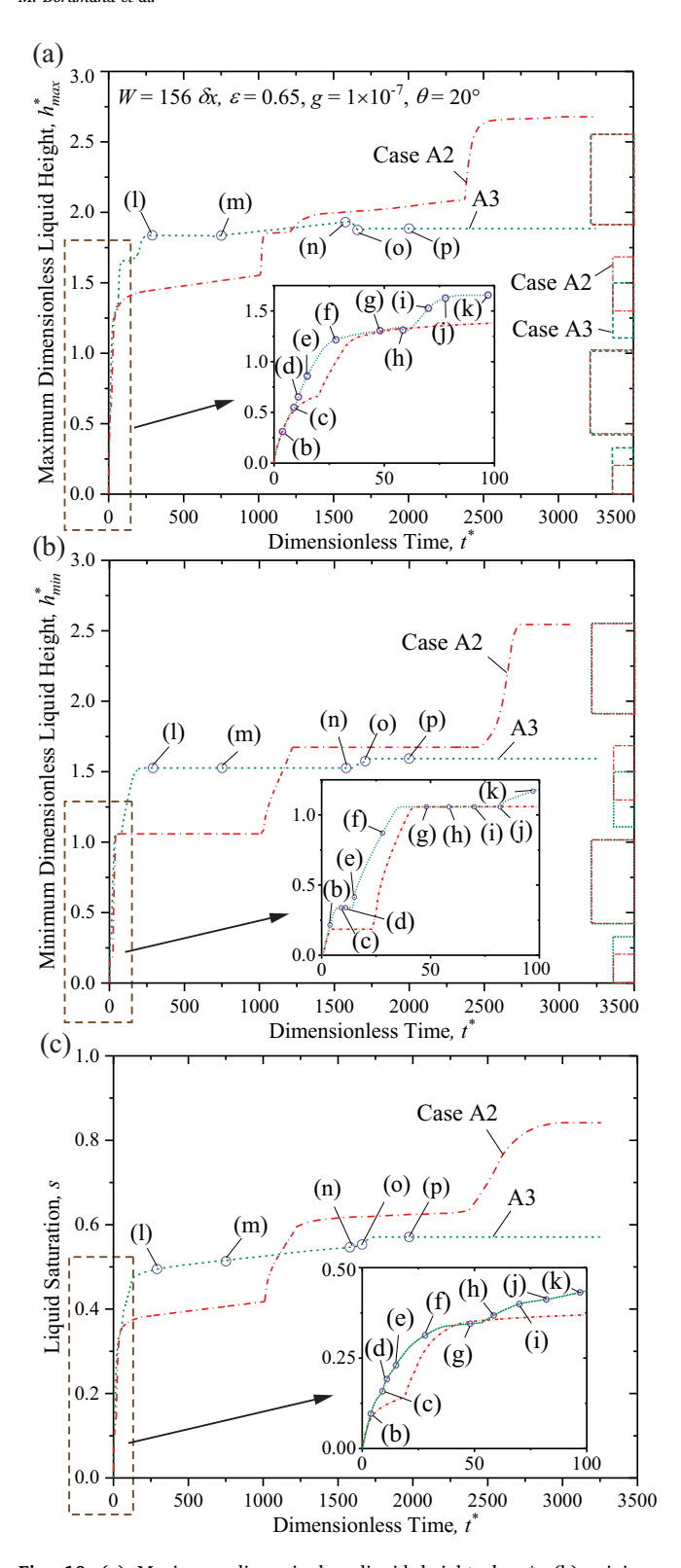


Fig. 10. (a) Maximum dimensionless liquid height, h_{max}^* , (b) minimum dimensionless liquid height, h_{min}^* , and (c) liquid saturation, s, as a function of dimensionless time, t^* , single-columnar BPSW with and without clustered-pores, i.e., Case A3 and A2, respectively, at given porosity $\varepsilon=0.65$ and parallel plate spacing W=156 δx .

rise from the first sharp capillary rise [point (q)] to equilibrium state [point (z_6)]. Point (r) shows the four menisci pinned. At $t^* = 5.6$, Fig. 11 (s) shows that the two outer menisci depin followed by the outer and inner menisci mergings which results in the formation of two new menisci at $t^* = 9.5$. At $t^* = 9.8$, Fig. 12(u)-(w) show the stronger meniscus-particle interaction at (u), the sharp capillary rise for the maximum height and the horizontal for the minimum height at (v), and the stick-slip flow at (w). Note that the minimum height, h_{min}^* , changes from the level of the top surface of the first-layer small particle to that of the top surface of the first-layer large particle between points (w). At t^* = 9.8, Fig. 12(x) shows the sharp capillary rise for the minimum height, followed by the meniscus-particle interaction at point (y) and sharp capillary rise at point (z). At $t^* = 22.7$, Fig. $12(z_1)$ shows both the maximum and minimum heights pin. At $t^* = 22.7$, Fig. $12(z_2)$ shows that the maximum height depins at $t^* = 110$, followed by the meniscus-particle interaction at $t^* = 291$, i.e., Fig. 12(z₃). At $t^* =$ 292-300, Fig. 12(z₄) and (z₅) show the horizontal/vertical sharp capillary rises.

At $t^*=300$, Fig. $12(z_5)$ shows that the maximum height reaches the top of the third-layer small particles, while the horizontally-flowing menisci merge, followed by the equilibrium state at $t^*=380$, Fig. $12(z_6)$. Note that the maximum height in Case B1 is larger than that of Case B0 due to the increased capillary rise momentum from the smaller pores, but the minimum height in Case B1 is slightly smaller that of Case B0 due to the pinning effect at the second-layer middle particle.

Fig. 13(a) compares the LBM predicted maximum dimensionless liquid heights, h_{max}^* , as a function of dimensionless time, t^* , for threecolumnar, UPSW (Case B0) and BPSW with small pore size ratio (Case B1) at given porosity $\varepsilon = 0.65$ and parallel plate spacing $W = 314 \delta x$. The time label used in Fig. 11 and Fig. 12, and the locations of the 4 particle layers (uniform or larger particles only) for Cases BO and B1, and the insets are also shown. The rate-of-rise for the maximum height of Case B1 vs. B0 is similar to that of A1 vs. A0. At t^* < 40, the two step-wise capillary rises, i.e., a sharp capillary rise followed by a plateau and another sharp capillary rise, are observed for both the maximum height of both cases, but for Case B1, the early capillary rise occurs at (v) to (w). This enhanced wickability is related to not only the increased local permeability from the large pores between the first-layer particle of Case B1 and the plates [see LP in Fig. 3(b)], but also the additional capillary rise momentum from the increased capillary pressure by the smaller pores between the second-layer particle of Case B1 and the plates [SP in Fig. 3(b)], i.e., the stronger interaction of the capillary meniscus front with the bottom corners of the particle at Fig. 12(u). At $40 < t^* < 291$, Case B1 continues to rise due to the larger capillary pumping from the small pore between the second-layer particle and the plates [SP in Fig. 3 (b)], while Case B0 reaches equilibrium height due to smaller capillary pressure. At $t^* > 291$, the Case B1 shows the additional sharp capillary rise, i.e., (z₄) and (z₅), due to the larger local permeability from the larger pores between the third-layer smaller particle and two plates, followed by the equilibrium height at the top of the third-layer particle, i.e., point (z₆). Fig. 13(b) compares the LBM predicted minimum dimensionless liquid heights, h_{min} *, as a function of dimensionless time, t*, for Case B1 compared to Case B0. The minimum height of Case B1 shows three step-wise rate-of-rise including sharp capillary rises and periods of no change, i.e., pinning. The minimum height of both Cases B1 and B2 reaches the level of the top surface of the second-layer particle, i.e., nearly same equilibrium height, however, since the top surface of the small second-layer particle, i.e., Case B1, is slightly below than that of the uniform second-layer particle, i.e., Case B0, the equilibrium height of Case B1 is slightly below than that of Case B0.

Fig. 13(c) compares the liquid saturation, s, as a function of dimensionless time, t^* , for Cases B0 and B1. Three significant liquid saturation increases of Case B1 are observed at points (u), (w), and (z₃). The first one is related to the larger local permeability from the large pores [LP in the bottom side of the BPSW followed by the strong capillary rise momentum from the meniscus-particle interaction at point (u)]. The second

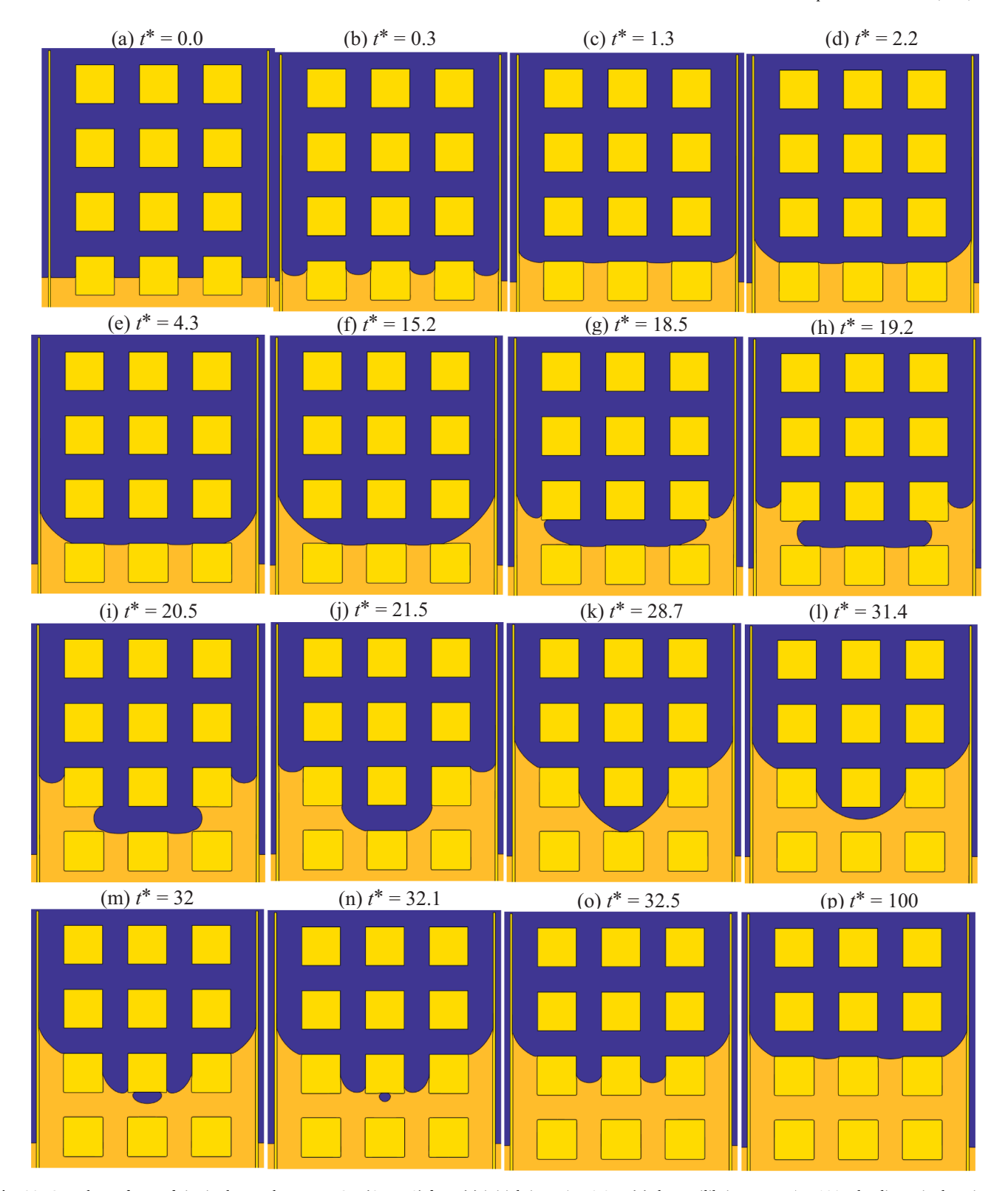


Fig. 11. Snapshots of rate-of-rise in three-columnar UPSW (Case B0) from (a) initial time, $t^* = 0.0$ to (p) the equilibrium state $t^* = 100$. The dimensionless time, t^* , corresponding to each snapshot is also shown.

one is related to the small pore size (in the diagonal direction) between the large particle in the first and second layer at point (w), and the third one is related to the large local permeability from the large pore between the third-layer small particle and the plates followed by large capillary pumping capability from the strong meniscus-particle interaction at point (z₃). The predicted maximum instantaneous and cumulative rate-

of-rise enhancements and capillary pressure enhancements of Case B1 using Eqs. (3) to (5) are ξ =285% (for h^*_{min} at t^* = 23), ω = 30% (in h^*_{max}), and γ = 54% (in h^*_{max}), and other detailed enhancement predictions and comparisons are summarized in Section 4.3.

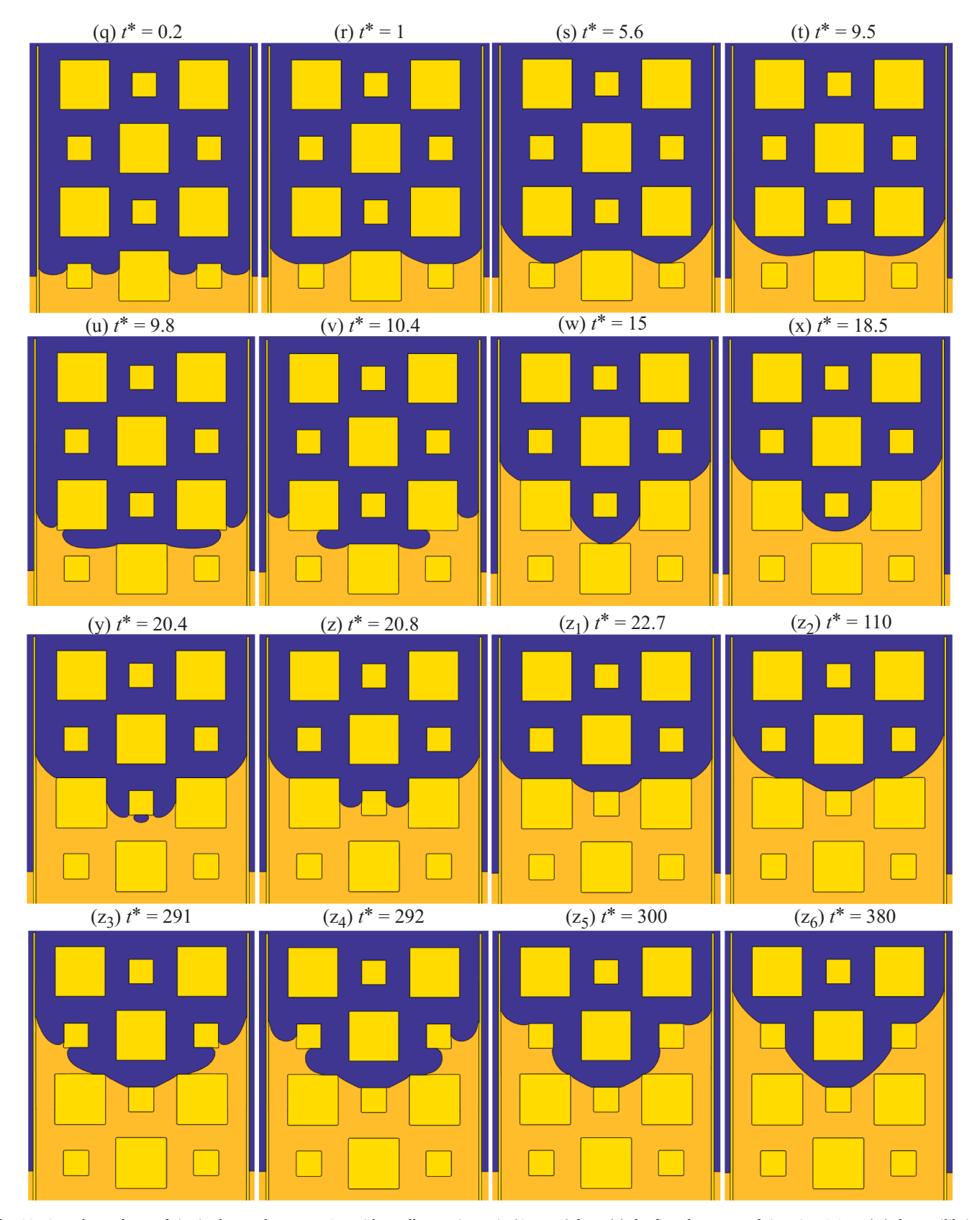


Fig. 12. Snapshots of rate-of-rise in three-columnar BPSW with small pore-size ratio (Case B1) from (q) the first sharp rate-of-rise, $t^* = 0.2$, to (z_6) the equilibrium state $t^* = 380$. The dimensionless time, t^* , corresponding to each snapshot is also shown.

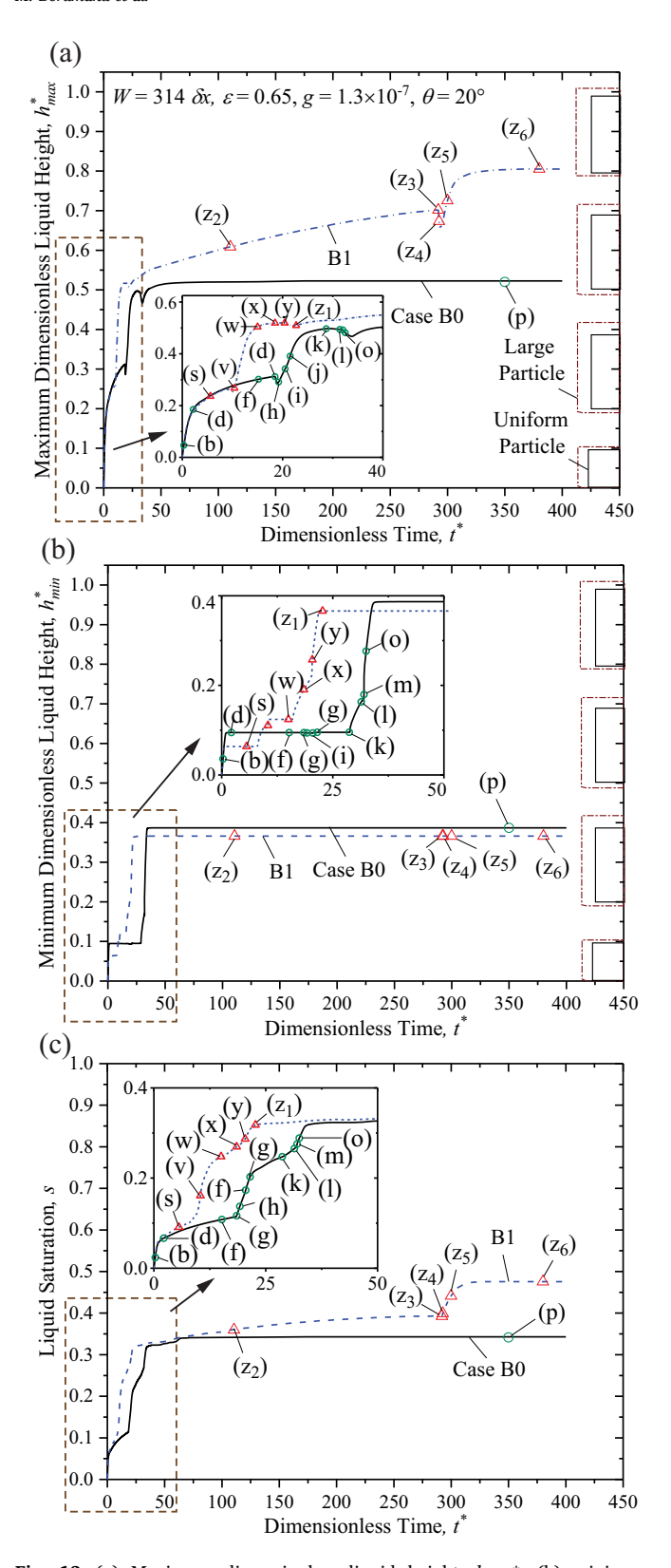


Fig. 13. (a) Maximum dimensionless liquid height, h_{max}^* , (b) minimum dimensionless liquid height, h_{min}^* , and (c) liquid saturation, s, as a function of dimensionless time, t^* , for three-columnar- UPSW (Case B0) and BPSW with small pore size ratio (Case B1) at given porosity $\varepsilon=0.65$ and parallel plate spacing $W=314~\delta x$.

4.2.2. BPSW with increased pore size ratio (Case B2)

This section studies the effects of the increased pore size ratio of the thee-columnar BPSW [Case B2, horizontally zig-zag arrangement, Fig. 3 (c)] on enhanced wickability by comparing the rate-of-rise with the three-columnar BPSW with small pore-size ratio [Case B1, Fig. 3(b)]. Fig. 14(a) shows the first sharp capillary rise at $t^* = 0.3$. At $t^* = 4.4$, Fig. 14(a) illustrates the significant liquid flow on the large pores [LP* in Fig. 3(c)], i.e., large permeability, and depinned meniscus on the small pore [SP* Fig. 3(c)], i.e., improved capillary pressure. Fig. 14(c) show the sharp capillary rise in vertical and horizontal directions. Fig. 14(d) shows that maximum height reaches the level of top surface of large second-layer particle while minimum height spreads over the top surface of the first-layer middle particle. This is followed by minimum height rise and meniscus-particle interaction at points (e) and (f), respectively. Fig. 14(g) and (h) show the sharp capillary rise in the central small and large pores, i.e., SP* and LP* in Fig. 3(c)]. At $t^* = 47.6$, Fig. 14(i) shows that the three menisci in the small pores are depinned due to the high capillary pressure while the small capillary pressure in the meniscus in the large pore (right meniscus in the center) cannot overcome the hydrostatic and pinning pressure, i.e., pinned. At $t^* = 143$, Fig. 14(j) shows that the small meniscus in the center has fully spread over the second-layer small particle, i.e., minimum height detachment. At 170 $< t^* < 174$, Fig. 14(k)-(l) show the early sharp capillary rise due to the small pore between the third-layer small particle and the plates [SP* in Fig. 3(c)]. Fig. 14(m)-(p) show the minimum height rise, meniscus-particle interaction, sharp capillary rise in the large pores [LP* in Fig. 3(c)], and the equilibrium state, respectively.

To understand the effects of increased pore size ratio on enhanced wickability of three-columnar BPSW, Fig. 15(a), (b), and (c) compare the LBM predicted maximum and minimum dimensionless liquid heights, h_{max}^* and h_{min}^* , and liquid saturation, s, respectively, as a function of dimensionless time, t^* , for three-columnar BPSW wicks with small (Case B1) and increased pore size ratio (Case B2, horizontal zig-zag particle rearrangement), at given porosity $\varepsilon=0.65$ and parallel plate spacing $W=314~\delta x$. The time labels used in Fig. 14, the location of the 4 large particles for Cases B1 and B2, and the insets are also shown.

In Fig. 15(a), i.e., h_{max} * vs t*, the large pores between the first-layer particle and the plates [LP* in Fig. 3(c)] improves the permeability at t^* = 6.5 [point (c)], the small pore between the second-layer particle and the plates provide capillary pumping capability until the maximum height reached point (d), then it slows down for an extended time period (points (i) to (j), i.e., stick-slip flow), and finally the small pore between the third-layer particle and the plates [SP* in Fig. 3(c)] provides the capillary pumping capability for the final sharp capillary rise until it reaches equilibrium state at point (p). In Fig. 15(b), i.e., h_{min} * vs t*, the improved minimum height between points (c) to (d) stems from the stronger horizontal capillary flow in the meniscus formed between the particles in the small particle in the first layer and the large particle in the second layer [compare point (c) in Fig. 14 with point (t) in Fig. 12]. The next major improvement in minimum height for Case B2 occurs at points (j) in which the central meniscus rises above the second-layer middle particle due to the high capillary pressure from the small pore between that particle and the left particle [SP* in Fig. 3(c)]. Note the distinction between this meniscus rise and the pinned meniscus in Case B1, i.e., Fig. $12(z_1)$ to (z_6) . The final sharp capillary rise for the minimum height occurs at points (m) to (n) where it finally reaches the level of the top surface of the third-layer small particles at point (p). The liquid saturation in Fig. 15(c) also shows the similar flow behavior, i.e., enhanced rate-of-rise at point (c) to (d) as well as capillary rise above those of Case B1 at points (m) to (p) due to the larger pore size ratio from the horizontal zig-zag arrangement of the small and large pores.

4.2.3. BPSW with clustered-pores

To understand the clustered-pore effects on enhanced wickability of three-columnar BPSW (Case B3, vertical/horizontal zig-zag particle rearrangement), the LBM predicted rate-of-rise is compared with that of

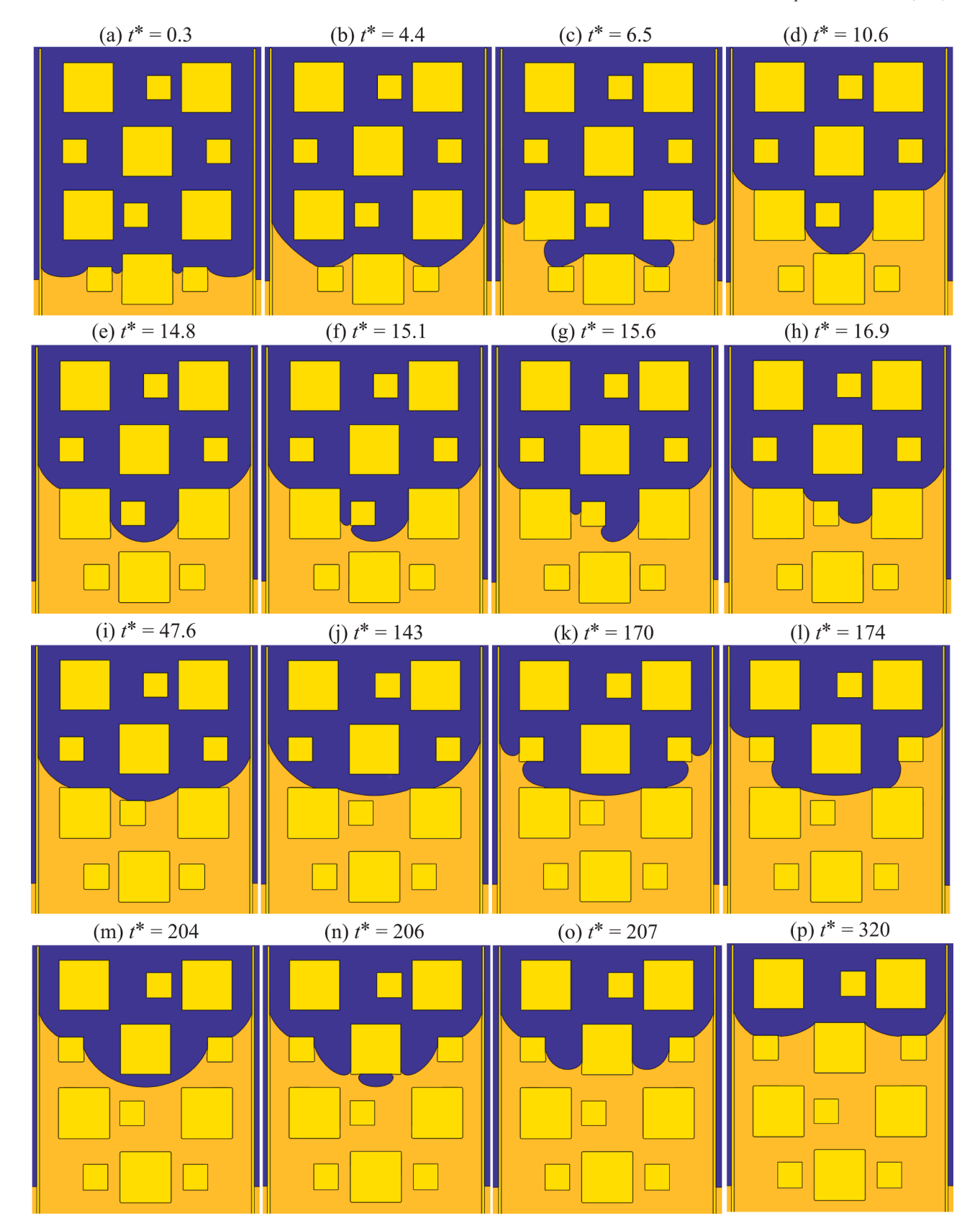


Fig. 14. Snapshots of rate-of-rise in three-columnar BPSW with increased pore-size ratio (Case B2) from (a) the first sharp rate-of-rise, $t^* = 0.3$, to (p) the equilibrium state $t^* = 320$. The dimensionless time, t^* , corresponding to each snapshot is also shown.

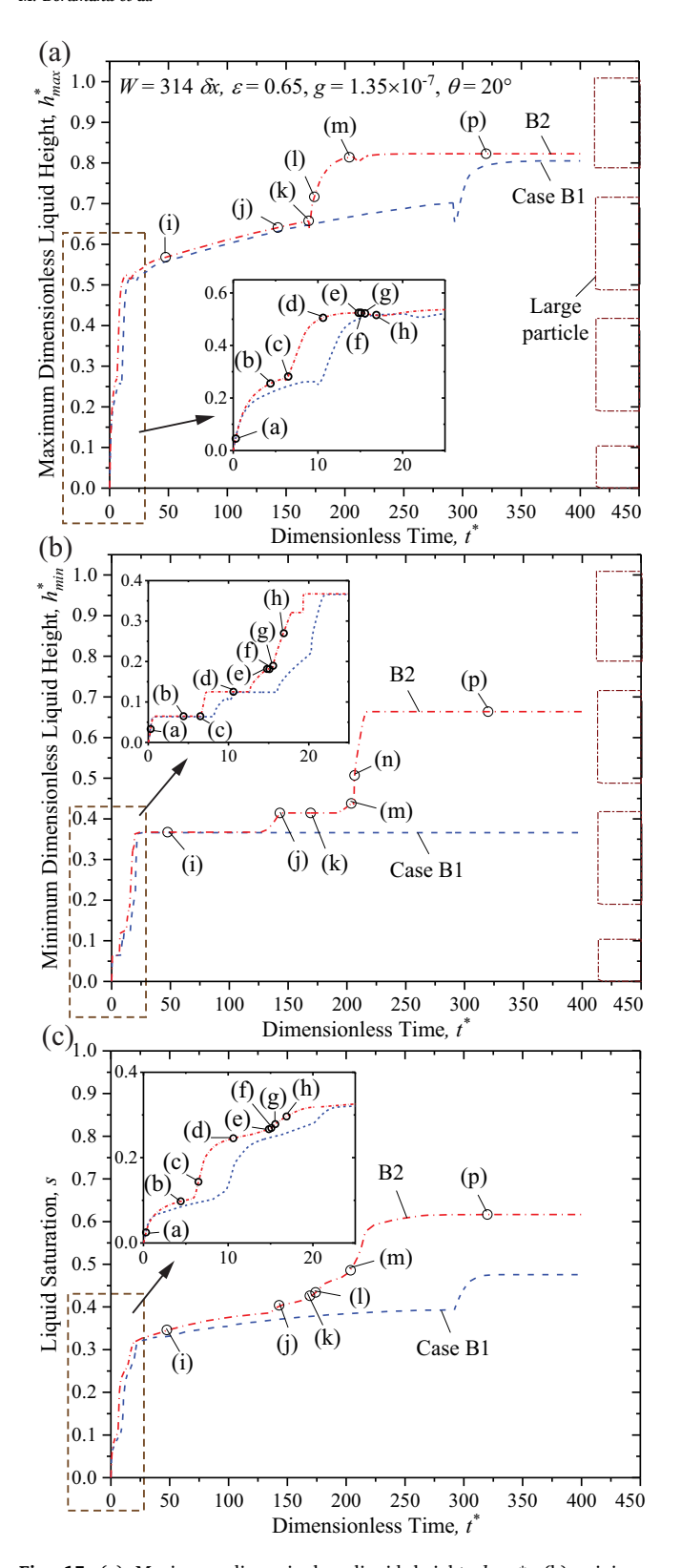


Fig. 15. (a) Maximum dimensionless liquid height, h_{max}^* , (b) minimum dimensionless liquid height, h_{min}^* , and (c) liquid saturation, s, as a function of dimensionless time, t^* , for three-columnar- BPSW with small and large poresize ratio, i.e., Cases B1 and B2, respectively, at given porosity $\varepsilon=0.65$ and parallel plate spacing W=314 δx .

Case B2, i.e., BPSW without clustered-pores (horizontal zig-zag particle rearrangement only). Fig. 16 shows the LBM simulation snapshots of the rate-of-rise from the initial time to equilibrium state for Case A3 [see Fig. 3(d)]. The main differences between the pore-scale capillary flow of Cases B3 and B2 are summarized below. Fig. 16(d) shows the early meniscus-particle interaction at $t^* = 2.3$ from the large local permeability of the large clustered-pores [LP** in Fig. 3(d)]. At $t^* = 6.9$, Fig. 16(g) shows the early sharp horizontal/vertical capillary flows due to the clusters of small pores [SP** in Fig. 3(d)] followed minimum height rise to the level of the top surface of the second-layer particles due to the large clustered-pores at $t^* = 46.6$, Fig. 16(g). Similarly, at $120 < t^*$ < 123, Fig. 16(l)-(m) show the early sharp horizontal/vertical capillary flow due to the clusters of small pores near the second- and third-layer particles and the plates. Fig. 16(n) shows the formation a new meniscus with large radius between the third-layer small particles followed by the final sharp capillary rise and equilibrium state at points

To further understand the effects of clustered-pores on enhanced wickability of BPSW, Fig. 17(a) to (c) compare the LBM predicted maximum and minimum dimensionless liquid heights, h_{max}^* and h_{min}^* , and liquid saturation, s, respectively, as a function of dimensionless time, t^* , for three-columnar BPSW with clustered-pores (Case B3, vertical/horizontal zig-zag particle rearrangement) and three-columnar BPSW without clustered-pores (Case B2, horizontal zig-zag particle rearrangement only), at given porosity $\varepsilon = 0.65$ and parallel plate spacing $W = 314 \delta x$. The time labels used in Fig. 16, the vertical location of the 4 large particles for Cases B3 and B2, and the insets are also shown. The enhanced liquid height and saturation observed in points (c)-(e) of Fig. 17 stem from the early meniscus-particle interaction at t^* = 2.3, i.e., point (d), compared with the snapshot at t^* = 4.4 in Fig. 14 (b). Furthermore, the small central clustered-pores [SP** in Fig. 3(d)] result in both vertical and horizontal capillary flows in points (g) to (h), compare with no horizontal capillary flow in Fig. 14(d) to (f), i.e., enhanced wickability for Case B3 compared to Case B2. The minimum height then pins at the top corner middle second-layer particle [point (j)]. The enhanced rate-of-rise at points (l) to (n) results from the clusters of small pores between the second-layer large, the third-layer small, and the plates [see SP** in Fig. 3(d)]. Finally, the capillary meniscus in the center continues to rise through the pores near the third-layer particles [points (n) and (o)], followed by reaching smaller equilibrium height at point (p), due to the large clustered-pore between the third- and fourthlayer particles [see LP** in Fig. 3(d)].

4.3. Summary of the enhanced wickability of single- and three-columnar BPSW

Using Eqs. (3) to (5), Table 4 summarizes the predicted enhanced wickability of the single- and three-columnar BPSWs. The wickability of each BPSW is compared with the corresponding reference cases, i.e., UPSWs, as well with the other BPSWs, e.g., A3 is compared with A0 as well as with A1 and A2.

Therefore, effects of the non-uniform pore size distribution in BPSWs, i.e., Cases A1 and B1, increased pore size ratio, i.e., Cases A2 and B2, and clustered-pores, i.e., Cases A3 and B3, on enhanced wickability are examined. Furthermore, Fig. 18 compares the LBM predicted liquid saturation, s, as a function of dimensionless time, t^* , for the (a) single-and (b) three-columnar BPSW, at given porosity $\varepsilon=0.65$. The insets in Fig. 18 magnify the early stages of the rate-of-rise for improved readability. The following can be concluded from Fig. 18.

- All the single- and three-columnar BPSWs enhance the local permeability and capillary pressure compared to the corresponding UPSW due to the non-uniform pore size distribution in the BPSW.
- For the first and second, step-wise sharp capillary rises, i.e., at $t^* < 100$ for single- and $t^* < 15$ for three-columnar wicks, the

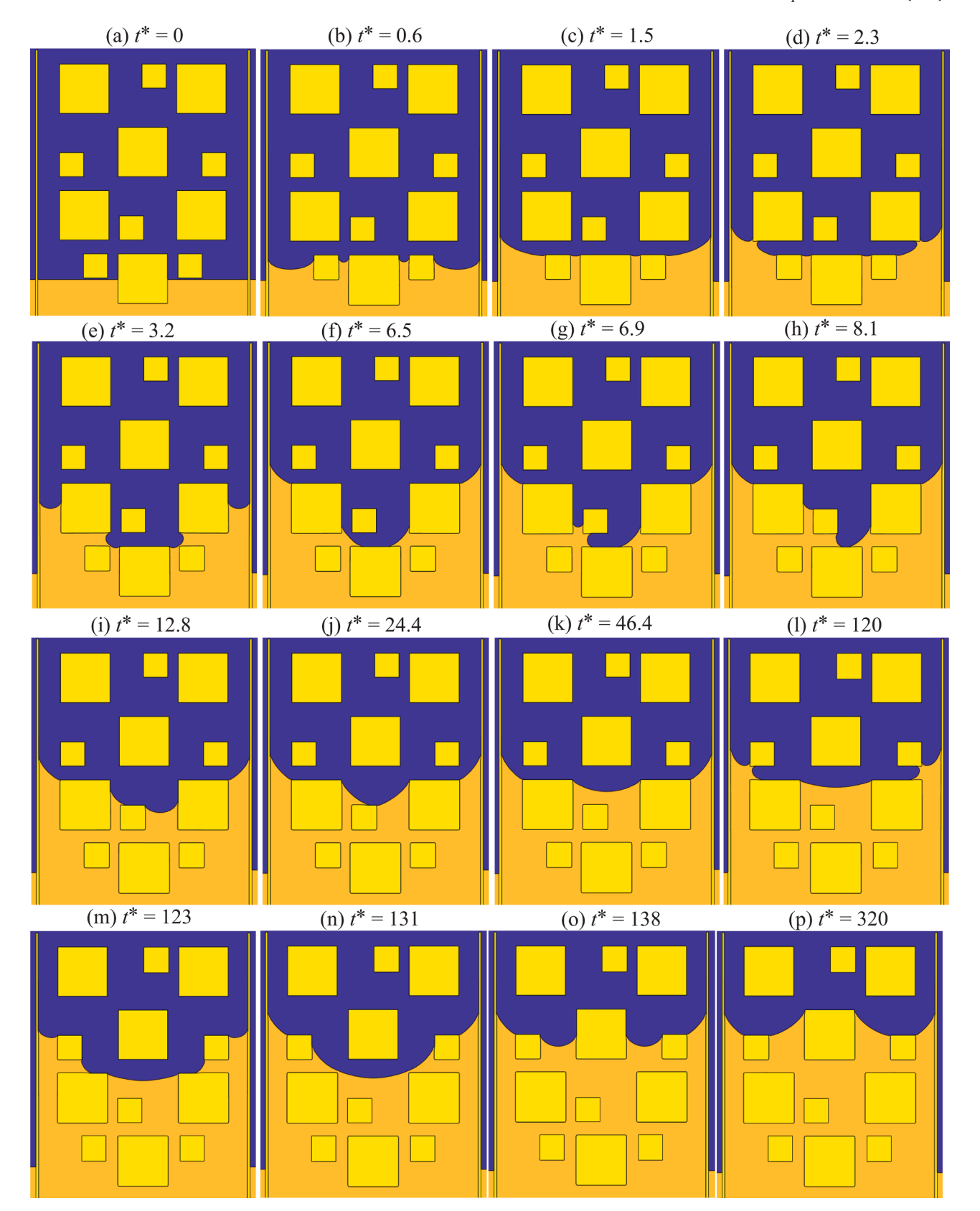


Fig. 16. Snapshots of rate-of-rise in three-columnar BPSW with clustered-pores (Case B3) from (a) the initial time, $t^* = 0$ to (p) the equilibrium state, i.e., $t^* = 320$. The dimensionless time, t^* , corresponding to each snapshot is also shown.

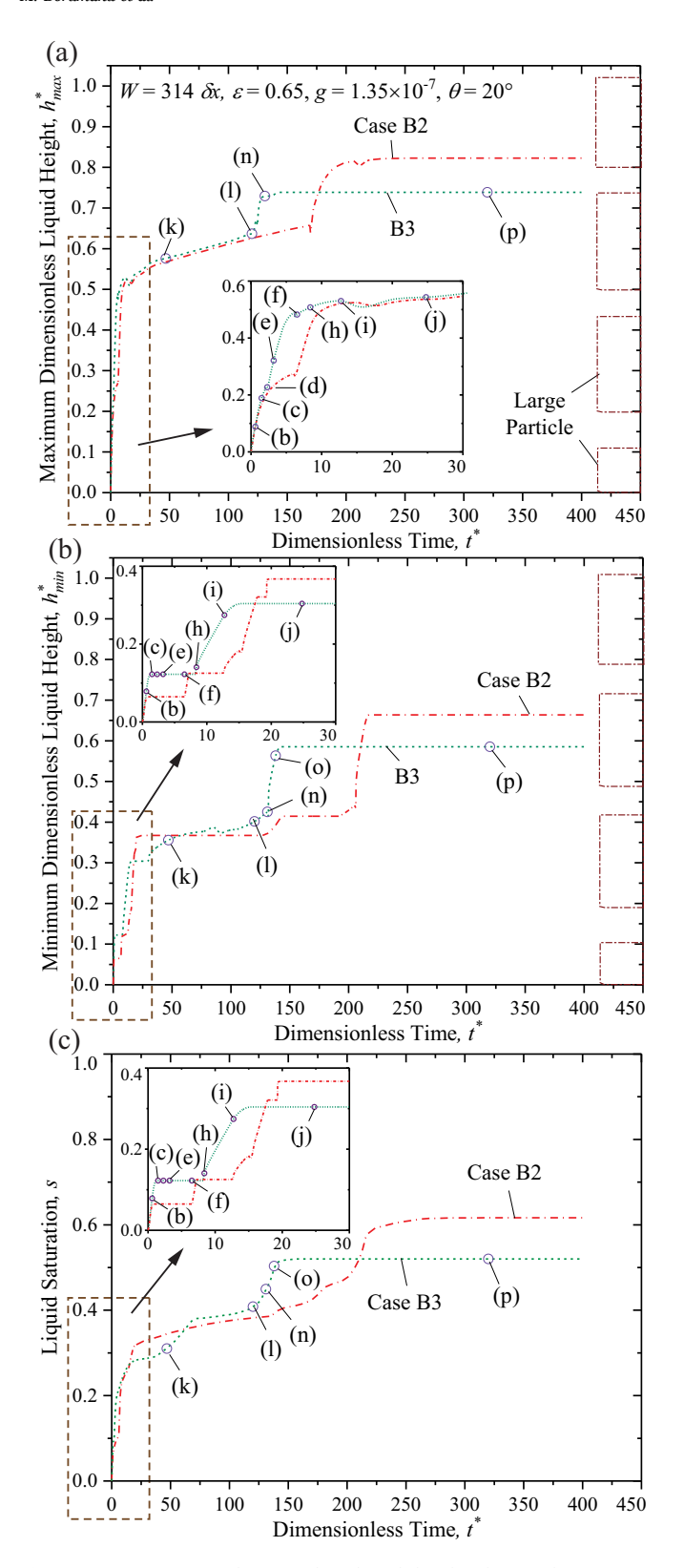


Fig. 17. (a) Maximum dimensionless liquid height, h_{max}^* , (b) minimum dimensionless liquid height, h_{min}^* , and (c) liquid saturation, s, as a function of dimensionless time, t^* , for three-columnar BPSW with and without clustered-pores, i.e., Case B3 and B2, respectively, at given porosity $\varepsilon=0.65$ and parallel plate spacing $W=156~\delta x$.

instantaneous wickability enhancements, ξ , are Cases A3 > A2 > A1 > A0, and similarly Cases B3 > B2 > B1 > B0.

- The capillary pressure enhancement of the clustered-pore BPSW is more pronounced for the three-columnar BPSWs compared to the single-columnar ones due to the increased smaller- and larger clustered-pore segregation, resulting in the enhanced equilibrium saturation $s_{\rm B3,\ eq} > s_{\rm B1,\ eq}$, while $s_{\rm A3,\ eq} < s_{\rm A1,\ eq}$.
- The maximum wickability enhancements are found in Cases A2 and B2, i.e., single- and three-columnar BPSW with increased pore size ratio, since the larger pores improve the local permeability by opening additional flow paths while the smaller pores further improve the capillary pressure. The predicted maximum instantaneous and cumulative rate-of-rise enhancements and capillary pressure enhancement are $\xi = 309\%$ (for h^*_{\min} at equilibrium, i.e., $t^* = 78$), $\omega = 74\%$ (in s), and $\gamma = 151\%$ (in h^*_{\min}) for Case A2 compared to Case A0 and $\xi = 295\%$ (for h^*_{\max} at $t^* = 20$), $\omega = 49\%$ (in s), and $\gamma = 80\%$ (in h^*_{\min}) for Case B2 compared to Case B0.
- Compared to the BPSWs with small pore size ratio, the BPSWs with clustered-pore significantly enhance the wickability during the first and second, step-wise sharp capillary rises, i.e., the maximum instantaneous enhancements of liquid saturation is 148 at $t^* = 22$ for Case A3 compared to Case A1, and 137 at $t^* = 5$ for Case B3 compared to Case B1, respectively. However, the cumulative rate-of-rise enhancement is negligibly small for the single-columnar BPSW, i. e., $\omega = 4\%$ for liquid saturation of Case A3 compared to Case A1, and moderate for the three-columnar BPSW, i.e., $\omega = 19\%$ for liquid saturation of Case B3 compared to Case B1.
- The wickability enhancement of three-columnar, clustered-pores BPSW becomes more pronounced compared to that of the singlecolumnar BPSW, since the small and large clustered-pores of the neighboring particle columns synergistically contributes to the wickability enhancement while the small clustered-pores provide the capillary pumping capability and the large clustered-pores improve the local permeability.

5. Conclusion

This study examines the enhanced wickability of the Bi-Particle-Size Wicks (BPSW) by employing the free-energy-based, single-component, two-phase Lattice Boltzmann Method (LBM). The single- and three-columnar, four-layer, square particles having two different sizes are distributed uniformly (Case A1 and B1, i.e., single- and three-columnar, respectively) and non-uniformly (Cases A2-A3 and B2-B3) within the two parallel plates and rate-of-rise is compared with those of the reference cases, i.e., Uniform-Particle-Size Wicks (UPSW, Cases A0 and B0). The enhanced wickability is predicted by calculating the instantaneous and time-integral enhancements of the liquid heights and saturation as well as the capillary pressure enhancement of the BPSW. The main conclusions are summarized below.

- The non-uniform pore-network through the bi-particle size of the BPSW enhances the wickability not only by improving the local permeability from the large pores up to 309 and 285% for the singleand three-columnar BPSW, respectively, and but also by increasing the capillary pumping capability from the small pores up to 76 and 54% for the single- and three-columnar BPSW, respectively.
- The increased pore size ratio further enhances the wickability by improving the permeability from the larger pores up to 465 and 119% for the single- and three-columnar BPSW, respectively, and by increasing the capillary pumping capability from the smaller pores up to 52 and 81% for the single- and three-columnar BPSW, respectively.
- The clustered-pores further enhance the local permeability from the clusters of large pores up to 293 and 117% for the single- and threecolumnar BPSW, respectively, while reduces the capillary pressure due to the larger pore sizes.

Table 4
Cumulative and maximum instantaneous rate-of-rise enhancements and capillary pressure (equilibrium height) enhancement of the maximum dimensionless liquid height, h^*_{max} , minimum dimensionless liquid height, h^*_{min} , and liquid saturation, s, for all the single- and three-columnar BPSWs. The dimensionless time, t^* , corresponding to each of the maximum instantaneous enhancements are also shown.

Case #	Maximum Instantaneous, ξ %		Cumulative, ω %			Capillary Pressure, γ %			
	h^*_{\max} at t^*	h^*_{\min} at t^*	s at t^*	h^*_{\max}	$h*_{\min}$	S	h^*_{\max}	$h*_{\min}$	S
A1 vs A0	117 at 111	309 at 78	137 at 62	42	44	53	58	65	76
A2 vs A0	133 at 110	309 at 78	185 at 40	62	52	74	113	151	143
A2 vs A1	130 at 41	465 at 44	131 at 38	14	6	13	35	52	38
A3 vs A0	177 at 110	320 at 84	197 at 31	50	55	60	50	57	65
A3 vs A1	133 at 26	465 at 44	148 at 22	6	8	4	-5	-5	-6
A3 vs A2	60 at 19	293 at 23	85 at 19	-7	2	-8	-29	-37	-32
A3 vs A2, $t^* < 1,000$	_	_	_	23	41	30	_	_	_
B1 vs B0	82 at 19	285 at 23	134 at 18	30	-3	18	54	-5	39
B2 vs B0	81 at 19	295 at 20	171 at 18	41	40	49	57	72	80
B2 vs B1	99 at 10	97 at 7	119 at 8	8	44	26	2	81	30
B3 vs B0	101 at 6	227 at 20	162 at 5	36	39	41	41	51	52
B3 vs B1	104 at 6	145 at 15	137 at 5	4	43	19	-2	60	9
B3 vs B2	81 at 6	117 at 13	107 at 5	-4	0	-5	-10	-12	-16
B3 vs B2, t* < 200	-	-	_	3	18	9	-	-	-

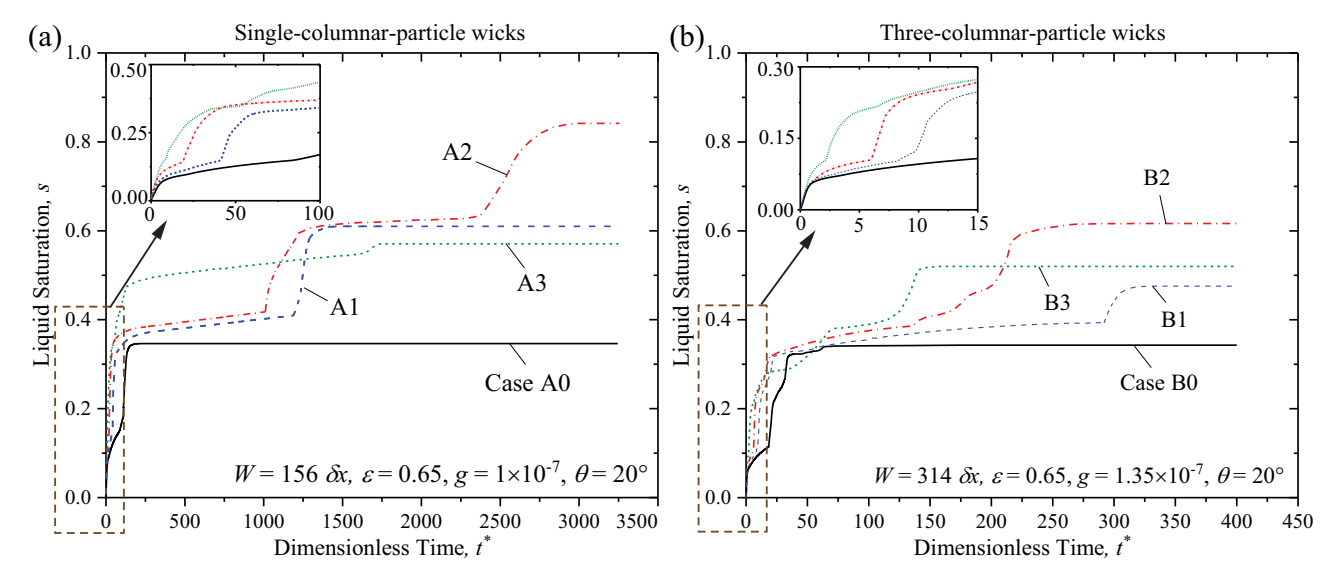


Fig. 18. Liquid saturation, s, as a function of dimensionless time, t^* , for all the (a) single-, and (b) three-columnar UPSW and BPSW, i.e., Cases A0-A3 and B0-B3, respectively, at given porosity $\varepsilon = 0.65$.

- The use of simple 2D square particles leads to sharp capillary rises followed by slow capillary rise due to the meniscus pinning and stickslip flow. The capillary pressure changes during the pining/depining/stick-slip flow processes can be further studied.
- The limitations of the current study are as follows. Firstly, the 2D wick with square particles may not fully reflect the realistic 3D porenetwork in practical wick structures. Furthermore, the liquid/vapor density ratio in TPTMS is typically larger than that of the current study ($\rho_l/\rho_v=5$). Finally, the isothermal LBM cannot examine the wickability enhancement under the phase-change phenomena. However, the obtained prediction results provide the insight into the wickability enhancement mechanisms of the single- and multicolumnar non-uniform pore wick without losing a capillary flow generality.
- The obtained 2D LBM simulation results for the enhanced wickability mechanism provide deep insights into the optimal 3D wick structural designs by elucidating the roles of the smaller and larger pores on the local permeability and capillary pressure.

CRediT authorship contribution statement

Mohammad Borumand: Methodology, Investigation, Software,

Writing – original draft. **Taehun Lee:** Methodology, Investigation, Software, Writing – review & editing. **Gisuk Hwang:** Conceptualization, Supervision, Funding acquisition, Writing – review & editing.

Declaration of Competing Interest

The authors declare that they have no known competing financial interests or personal relationships that could have appeared to influence the work reported in this paper.

Data availability

Data will be made available on request.

Acknowledgements

MB and GS are thankful for financial support by the National Science Foundation (NSF), Award No. OIA-1929187, and the Wichita State University Convergence Sciences Initiative Program, and the College of Engineering, Department of Mechanical Engineering, Wichita State University.

References

- [1] Mudawar I. Assessment of high-heat-flux thermal management schemes. IEEE Trans Compon Packag Technol 2001;24:122-41. https://doi.org/10.1109/ 6144.926375.
- Egbo M, Borumand M, Nasersharifi Y, Hwang G. Surface orientation effects on pool-boiling with plain and enhanced surfaces. Appl Therm Eng 2021:117927.
- Borumand M., Hwang G. High heat flux two-phase thermal control system using non-uniform capillary evaporator(ICES-2019-176) 2019, 49th International Conference on Environmental Systems, Boston, MA, USA.
- Mehdi S, Shah Y, Kim N-H. Bubble dynamics of R-123 and R-134a on pore/subtunnel surfaces. Int J Therm Sci 2022;177:107543.
- [5] Xiao B, Wang W, Zhang X, Long G, Fan J, Chen H, et al. A novel fractal solution for permeability and Kozeny-Carman constant of fibrous porous media made up of solid particles and porous fibers. Powder Technol 2019;349:92–8. https://doi.org/ 10.1016/i.powtec.2019.03.028
- [6] Liang M, Fu C, Xiao B, Luo L, Wang Z. A fractal study for the effective electrolyte diffusion through charged porous media. Int J Heat Mass Transf 2019;137:365-71.
- [7] Faghri A. Heat pipe science and technology. Global Digital Press; 1995.
- [8] Faghri A. Review and advances in heat pipe science and technology. J Heat Transf 2012:134, https://doi.org/10.1115/1.4007407
- [9] Tang Y, Tang H, Li J, Zhang S, Zhuang B, Sun Y. Experimental investigation of capillary force in a novel sintered copper mesh wick for ultra-thin heat pipes. Appl Therm Eng 2017;115:1020-30. https://doi.org/10.1016/j. pplthermaleng 2016 12 056
- [10] Experimental study on the heat transfer performance of ultra-thin flattened heat pipe with hybrid spiral woven mesh wick structure - ScienceDirect n.d. https:// ww.sciencedirect.com/science/article/pii/S1359431119337123?casa_token=cQ -aOnrUjkYAAAAA:mfP8Hx-hg7IU4-TnZqdEhemCQevEG0tobBK0qtrdGSgmT fVzx8Vqz2450dZSVjex63Sq-MJ4fQ [Accessed 16 February 2022).
- [11] Kim SJ, Ki Seo J, Hyung Do K. Analytical and experimental investigation on the operational characteristics and the thermal optimization of a miniature heat pipe with a grooved wick structure. Int J Heat Mass Transf 2003;46:2051-63. http loi.org/10.1016/S0017-9310(02)00504-5
- [12] Chen S-W, Hsieh J-C, Chou C-T, Lin H-H, Shen S-C, Tsai M-J. Experimental investigation and visualization on capillary and boiling limits of micro-grooves made by different processes. Sens Actuators Phys 2007;139:78-87. https:// rg/10.1016/i.sna.2007.03.009.
- [13] Holley B, Faghri A. Permeability and effective pore radius measurements for heat pipe and fuel cell applications. Appl Therm Eng 2006;26:448-62. https://doi.org/ 10.1016/i.applthermaleng.2005.05.023
- [14] Deng D, Liang D, Tang Y, Peng J, Han X, Pan M. Evaluation of capillary performance of sintered porous wicks for loop heat pipe. Exp Therm Fluid Sci 2013;50:1-9. https://doi.org/10.1016/j.expthermflusci.2013.04.014.
- Byon C, Kim SJ. The effect of the particle size distribution and packing structure on the permeability of sintered porous wicks. Int J Heat Mass Transf 2013;61: 499-504. https://doi.org/10.1016/j.ijheatmasstransfer.2013.02.025
- Byon C, Kim SJ. Capillary performance of bi-porous sintered metal wicks. Int J Heat Mass Transf 2012;55:4096-103. https://doi.org/10.1016/ heatmasstransfer.2012.03.051.
- [17] Effects of pore structure characteristics on performance of sintered bi-porous Ti3AlC2 wicks - IOPscience n.d. https://iopscience.iop.org/article/10.1088/20 53-1591/abdcfa/meta [Accessed 20 February 20 2022].

- [18] Egbo M, Keese J, Hwang G. Enhanced wickability of bi-particle-size, sinteredparticle wicks for high-heat flux two-phase cooling systems. Int J Heat Mass Transf 2021;179:121714. https://doi.org/10.1016/j.ijheatmasstransfer.2021.121714
- [19] Krastev VK, Falcucci G. Simulating engineering flows through complex porous media via the lattice Boltzmann method. Energies 2018;11:715. https://doi.org/ 10.3390/en11040715.
- Raeini AQ, Blunt MJ, Bijeljic B. Modelling two-phase flow in porous media at the pore scale using the volume-of-fluid method. J Comput Phys 2012;231:5653-68. ttps://doi.org/10.1016/j.jcp.2012.04.011.
- [21] Nikkhah A., Karami N., Tessier-Poirier A., Abouali O., Fréchette L.G. CFD Modelling of film deposition from a receding meniscus in a capillary tube using the approach of overset grid technique, 2022. https://doi.org/10.11159/ffhmt22.211.
- Akhlaghi Amiri HA, Hamouda AA. Evaluation of level set and phase field methods in modeling two phase flow with viscosity contrast through dual-permeability porous medium. Int J Multiph Flow 2013;52:22-34. https://doi.org/10.1016/j. ijmultiphaseflow.2012.12.006
- [23] Huang H, Huang J-J, Lu X-Y. Study of immiscible displacements in porous media using a color-gradient-based multiphase lattice Boltzmann method. Comput Fluids 2014;93:164–72. https://doi.org/10.1016/j.compfluid.2014.01.02
- Lattice Boltzmann simulation of pressure-driven two-phase flows in capillary tube and porous medium - ScienceDirect n.d. https://www.sciencedirect.com/science/ article/pii/S0045793017302025?casa_token=hDUSc_jtAWwAAAAA:Bta10 mzQNX459ciCw2P4BYjPE1zwqb8RgBUqOMMDjexcrRVzVapZuF6GM_yw3 5dVR2N0qQUgpw [Accessed 21 February 2022].
- [25] Liu H, Valocchi AJ, Kang Q, Werth C. Pore-scale simulations of gas displacing liquid in a homogeneous pore network using the Lattice Boltzmann method. Transp Porous Media 2013;99:555-80. https://doi.org/10.1007/s11242-013-020
- Liu H, Zhang Y, Valocchi AJ. Lattice Boltzmann simulation of immiscible fluid displacement in porous media: homogeneous versus heterogeneous pore network. Phys Fluids 2015;27:052103. https://doi.org/10.1063/1.4921611.
- Li J, Zheng W, Su Y, Hong F. Pore scale study on capillary pumping process in three-dimensional heterogeneous porous wicks using Lattice Boltzmann method. Int J Therm Sci 2022;171:107236. https://doi.org/10.1016/j. ijthermalsci.2021.107236.
- Borumand M, Lee T, Hwang G. Enhanced wickability of single-columnar, nonuniform pore-size wick using Lattice Boltzmann Method. Comput Fluids 2022;238: 105376. https://doi.org/10.1016/j.compfluid.2022.105376.
- [29] Faghri A. Heat pipe science and technology. Taylor & Francis; 1995
- [30] Borumand M, Lee T, Hwang G. Enhanced wickability of thin non-uniform sintered particle wicks using lattice Boltzmann method. American Society of Mechanical Engineers Digital Collection; 2021. https://doi.org/10.1115/IMECE2020-24311.
- Lee T, Lin C-L. A stable discretization of the lattice Boltzmann equation for simulation of incompressible two-phase flows at high density ratio. J Comput Phys 2005;206:16-47. https://doi.org/10.1016/j.jcp.2004.12.001.
- Lee T, Fischer PF. Eliminating parasitic currents in the lattice Boltzmann equation method for nonideal gases. Phys Rev E 2006;74. https://doi.org/10.1103/
- Lee T, Liu L. Wall boundary conditions in the lattice Boltzmann equation method for nonideal gases. Phys Rev E 2008;78:017702. https://doi.org/10.1103/ PhysRevE 78 017702
- Connington K, Lee T. Lattice Boltzmann simulations of forced wetting transitions of drops on superhydrophobic surfaces. J Comput Phys 2013;250:601-15. https://doi.org/10.1016/j.com/phys/10.101 doi.org/10.1016/j.jcp.2013.05.012.[35] Wiklund HS, Uesaka T. Microfluidics of imbibition in random porous media. Phys
- Rev E 2013;87:023006. https://doi.org/10.1103/PhysRevE.87.023006.